TRELLIS CODE-AIDED HIGH-RATE DIFFERENTIAL SPACE-TIME BLOCK CODE AND ENHANCED UNCODED SPACE-TIME LABELING DIVERSITY

Buthanani Dlodlo

Supervisor: Professor Hongjun Xu

School of Engineering, Electrical, Electronic and Computer Engineering, University of KwaZulu-Natal, Durban, South Africa

Submitted in fulfilment of the degree of Master of Science in Engineering,

December 2017

As the candidate's supervisor, I agree to the submission of this dissertation.

Date of Submission: _____

Supervisor: _____

Professor Hongjun Xu

Declaration 1 - Plagiarism

I, Dlodlo Buthanani, declare that:

1. The research reported in this thesis, except where otherwise denoted, is my original research.
2. This thesis has not been submitted for any degree or examination at any other university.
3. This thesis does not contain other persons' data, pictures, graphs or other information, unless specifically acknowledged as being sourced from other persons.
4. This thesis does not contain other persons' writing, unless specifically acknowledged as being sourced from other researchers. Where other written sources have been quoted, then:
    a. Their words have been re-written but the general information attributed to them has been referenced
    b. Where their exact words have been used, then their writing has been placed in italics and inside quotation marks, and referenced.
5. This thesis does not contain text, graphics or tables copied and pasted from the Internet, unless specifically acknowledged, and the source being detailed in the thesis and in the References sections.

Signed: _____

Declaration 2 - Publications

DETAILS OF CONTRIBUTION TO PUBLICATIONS that form part and/or include research presented in this dissertation (include publications in preparation, submitted, *in press* and published and give details of the contributions of each author to the experimental work and writing of each publication)

Publication 1:

B. Dlodlo, H. Xu and N. Pillay, "Bandwidth Efficiency Improvement for Differential Alamouti Space-time Block Codes using M-QAM," November 2017. An exposition of the main idea of this publication is given in Chapter 3 of this dissertation.

Submitted to SAIEE Africa Research Journal

Publication 2:

B. Dlodlo and H. Xu, "Performance Analysis of High-rate M-QAM Uncoded Space-time Labeling Diversity," October 2017. An exposition of the main idea of this publication is given in Chapter 4 of this dissertation.

Submitted to International Journal of Communication Systems

Signed: _____

Acknowledgements

My sincere gratitude goes to my supervisor, Professor Hongjun Xu, for his encouragement, expert advice and guidance. I have learnt a lot from him regarding academic writing, research and diligence. My gratitude also goes to Dr Narushan Pillay, who played a significant role in helping me to improve my academic writing skills. Lastly I would like to thank my employer and sponsor, the National University of Science and Technology for the financial support and the opportunity to develop myself further. Glory be to the Creator.

Abstract

In this dissertation, a trellis code-aided bandwidth efficiency improvement technique for space-time block coded wireless communication systems is investigated. The application of the trellis code-aided bandwidth efficiency improvement technique to differential space-time block codes (DSTBC) results in a high-rate system called trellis code-aided DSTBC (TC-DSTBC). Such a system has not been investigated in open literature to date. Hence, in this dissertation, the mathematical models and design methodology for TC-DSTBC are presented.

The two transmit antenna TC-DSTBC system transmits data by using a transmission matrix similar to the conventional DSTBC. The fundamental idea of TC-DSTBC is to use a dynamic mapping rule rather than a fixed one to map additional bits onto the expanded space-time block code (STBC) prior to differential encoding, hence, the additional bits-to-STBC mapping technique, which incorporates trellis coding is proposed for square M-ary quadrature amplitude modulation (M-QAM) in order to enhance the bandwidth efficiency without sacrificing the error performance of the conventional DSTBC. The comparison of bandwidth efficiency between TC-DSTBC and the conventional DSTBC show that TC-DSTBC achieves a minimum of 12.5% and 8.3% increase in bandwidth efficiency for 16-QAM and 64-QAM, respectively. Furthermore, the Monte Carlo simulation results show that, at high signal-to-noise ratios (SNR), the four receive antenna TC- DSTBC retains the bit error rate (BER) performance of the conventional DSTBC with the same number of receive antennas under the same independent and identically distributed (i.i.d.) Rayleigh frequency-flat fading channel and additive white noise (AWGN) conditions for various square M-QAM modulation orders and numbers of additional bits.

Motivated by the bandwidth efficiency advantage of TC-DSTBC over the conventional DSTBC, the trellis code-aided bandwidth efficiency improvement technique is extended to the recently developed uncoded space-time labeling diversity (USTLD) system, where a new system referred to as enhanced uncoded space-time labeling diversity (E-USTLD) is proposed. In addition to this, a tight closed form lower-bound is derived to predict the average BER of the E-USTLD system over i.i.d. Rayleigh frequency-flat fading channels at high SNR. The Monte Carlo simulation results validate that the more bandwidth efficient four receive antenna E-USTLD system at the minimum retains the BER performance of the conventional four receive antenna USTLD system under the same fading channel and AWGN conditions for various square M-QAM modulation orders.

The bandwidth efficiency improvement for TC-DSTBC and E-USTLD is achieved at the cost of a much higher computational complexity at the receiver due to use of the high-complexity Viterbi algorithm (VA)-based detector. Therefore, the low-complexity (LC) near-maximum-likelihood (near-ML) detection scheme proposed for the conventional USTLD is extended to the E-USTLD

detector in order to reduce the magnitude of increase in the computational complexity. The Monte Carlo simulation results show that E-USTLD with a VA-based detector that implements LC near-ML detection attains near optimal BER performance.

Table of Contents

List of Figures

List of Tables

List of Acronyms

AWGN……..……..Additive White Gaussian Noise

BEP……...Bit Error Probability

BER…….Bit Error Rate

BI-STCM……Bit Interleaved Space-time Coded Modulation

CDD…….Conventional Differential Detection

CDD-DSTBC..Conventional Differential Detection-aided Differential Space-time Block Code

CSI……...Channel State Information

DSTBC……..….. Differential Space-time Block Code

EI…….……..Efficiency Improved

E-USTLD…….……..…..Enhanced Uncoded Space-time Labeling Diversity

FSK……...Frequency Shift Keying

HC……..…..……...…….……High-complexity

i.i.d.……...……..Independent and Identically Distributed

LC……..…..……Low-complexity

MIMO….……...……..Multiple-Input Multiple-Output

MS…….…….…...……...……..Modulation Schemes

MGF...…….……Moment Generating Function

ML…….…….…….…….....…….Maximum-likelihood

MLSE…….....Maximum-Likelihood Sequence Estimation

M-PSK…….…….……M-ary Phase Shift Keying

M-QAM……...M-ary Quadrature Amplitude Modulation

OP……...……Orthogonal Projection

PAPR……..……..….Peak-to-Average Power Ratio

PDF……..…….Probability Distribution Function

PEP……..…….Pairwise Error Probability

PSK……..……..…...……...Phase Shift Keying

QPSK……...….Quadrature Phase Shift Keying

RF…….…...…….Radio Frequency

RV……..Random Variable

SM…….……..…….Spatial Modulation

SNR…….……Signal-to-Noise Ratio

STBC…….……..…. Space-time Block Code

STBC-SM……..……. Space-time Block Coded Spatial Modulation

STBC-SM-LD……...…. Space-time Block Coded Spatial Modulation with Labeling Diversity

STCM…….…….Space-time Channel Modulation

TCM……..…….Trellis Coded Modulation

TC-DSTBC…….……Trellis Code-aided Differential Space-time Block Code

USTLD…….…….Uncoded Space-time Labeling Diversity

VA……..……Viterbi Algorithm

1. Introduction

Exponential growth in the demand for high data rate wireless communications requires communication systems to be more efficient and reliable. Reliable high data rate communications have been achieved by employing space-time block code (STBC)-based multiple-input multiple-output (MIMO) systems [1]. The strength of STBCs lies in the usage of diverse received versions of the same signal to mitigate the impairments of wireless multipath fading channels, hence, the full diversity orthogonal STBC first proposed by Alamouti has been extended to more reliable schemes with more than two transmit antennas. The orthogonality of the Alamouti STBC ensures decoupling of signals at the receiver of the STBC system with coherent detection [2].

Coherent detection requires high-complexity channel estimation, whose complexity increases with the number of receive antennas [3]. An increase in channel estimation complexity reduces the power efficiency, which can lead to poor battery life and durability in battery operated wireless communication systems. Hence, a differential detection scheme known as conventional differential detection (CDD) was developed, initially for differential STBC (DSTBC) using M-ary phase shift keying (M-PSK) [4], and later for DSTBC using M-ary quadrature amplitude modulation (M-QAM) [3]. The CDD scheme proposed in [3] also eliminates the fading channel power estimation requirement. However, the CDD-aided DSTBC (CDD-DSTBC) system incurs a signal-to-noise ratio (SNR) penalty. In order to improve the error performance of CDD-DSTBC, a number of schemes has been investigated in [3,5-7]. In spite of error performance advantages, the investigated differential schemes have low bandwidth efficiency. Several bandwidth efficiency improvement techniques have been investigated in order to enhance the bandwidth efficiency of STBC-based MIMO systems, an example of one popular technique is the unitary expansion technique, which expands the orthogonal STBC via unitary matrix transformation [8].

STBC expansion via unitary transformation increases the cardinality of space-time codes, where each space-time code is capable of conveying a unique pattern of additional bits. The impact of the unitary expansion technique has been an increase in the bandwidth efficiency and the bit error rate (BER) performance improvement of the orthogonal STBC with four transmit antennas [8]. However, the application of the unitary expansion technique to the conventional Alamouti STBC results in a system that has a degraded error performance. Furthermore, as the bandwidth efficiency is increased the error performance becomes increasingly degraded [8]. Therefore, the high-rate Alamouti STBC that employs the unitary expansion technique cannot be considered as the best candidate for meeting requirements of future wireless communications.

In this dissertation, we propose a trellis code-aided bandwidth efficiency improvement technique for M-QAM DSTBC with two transmit antennas that results in a system called trellis code-aided

DSTBC (TC-DSTBC). We also extend the proposed trellis code-aided bandwidth efficiency improvement technique to the recently developed uncoded space-time labeling diversity (USTLD) that results in a system referred to as enhanced USTLD (E-USTLD). Effectively, we propose TC-DSTBC and E-USTLD as possible candidates to meet requirements of future wireless communications.

1.1 Notation

N_{T} and N_{R} are numbers of transmit and receive antennas, respectively. Bold upper case and lower case letters are used for matrices and vectors, respectively. $|\cdot|$ and $\|\cdot\|_F$ represent the Euclidean and Frobenius norm operations, respectively. $\mathrm{E}\{\cdot\}$ is the expectation operator. $(\cdot)^*$ and $(\cdot)^H$ are the conjugate and the Hermitian transpose operator, respectively. d is the number of additional bits sent with each transmitted high-rate STBC compared to the conventional Alamouti STBC. $\mathbb{C}^{M\times N}$ is a set of $M \times N$ complex-valued matrices. $\mathbb{Z}_{\geq 0}$ is a set of non-negative integers including 0. argmin_{ω} represents the argument of the minimum with respect to ω. D is the bit delay. $\binom{n}{k}$ and $\lfloor z \rfloor$ represent the binomial coefficients and the largest integer less than or equal to z, respectively. The label D^{-1} indicates the transmission delay for one block. $\boldsymbol{I}_N$ is the $N \times N$ identity matrix. M is the modulation order.

1.2 A Brief Review on Bandwidth Efficiency Improvement Techniques

In this section, bandwidth efficiency is briefly discussed together with several bandwidth efficiency improvement techniques that are employed in STBC wireless communication systems. Furthermore, since a new bandwidth efficiency improvement technique for STBC wireless communication systems is presented in this dissertation, it is logical to survey some of the existing bandwidth efficiency improvement techniques for comparison purposes.

1.2.1 Bandwidth Efficiency

Bandwidth efficiency is defined as the rate of information transmission per unit channel bandwidth and is expressed in bits per second per Hz (b/s/Hz) [9]. Modulation schemes (MS) and the SNR are the dominant factors that affect the bandwidth efficiency of a wireless communication system [9]. In general, the bandwidth efficiency of a full-rate (rate 1) wireless communication system is expressed as $\log_2 M$ b/s/Hz since the baud (symbol rate) and the ideal minimum Nyquist channel bandwidth are considered to have the same value for most MS except frequency shift keying (FSK). The bit rate is mathematically defined as the product of the baud and $\log_2 M$, hence, dividing the bit rate by the bandwidth yields $\log_2 M$. The bandwidth efficiency can be increased beyond $\log_2 M$ b/s/Hz with the aid of bandwidth efficiency improvement techniques.

1.2.2 Bandwidth Efficiency Improvement Techniques

Bandwidth efficiency improvement techniques are employed in STBC wireless communication systems to increase the rate of information that can be transmitted over the limited bandwidth in order to efficiently utilise the available usable spectrum and hence, allow communication systems to accommodate more users or increase data rates available to each user. Some bandwidth efficiency improvement techniques employ expanded signal constellations, expanded space-time codes or extend signals to the spatial domain in order to convey additional bits. STBC transmission schemes that employ some of the bandwidth efficiency improvement techniques are briefly discussed below.

1.2.2.1 Space-Time Block Coded Spatial Modulation

Spatial modulation (SM) is a low-complexity (LC) MIMO transmission technique that enhances bandwidth efficiency by employing active antenna indices to convey additional information [10]. SM has been extended to STBC to enhance the bandwidth efficiency of Alamouti STBC. The resulting scheme, Alamouti space-time block coded spatial modulation (STBC-SM) also exploits the advantages of both the STBC and SM by introducing transmit diversity to improve the BER performance of SM. Alamouti STBC-SM is an $N_{\mathrm{T}} \times N_{\mathrm{R}}$ system with c possible transmit antenna pair combinations, where $c = \left\lfloor \binom{N_{\mathrm{T}}}{2} \right\rfloor_{2^p}$ and p is a positive integer [10]. A bit stream consisting of $\log_2 c + 2\log_2 M$ random bits is fed into the STBC-SM transmitter to select a pair of Gray-coded MS symbols and activate one pair of the c transmit antenna pair combinations for transmission. At the receiver, it is assumed that full channel knowledge is available. The maximum-likelihood (ML) detector jointly estimates antenna pair index and symbol indices by performing an exhaustive search over all cM^2 possible antenna pair and symbol pair combinations [10]. However, the limitation on the practical number of transmit antennas that can be used may limit the STBC-SM from achieving high bandwidth efficiencies.

1.2.2.2 Space-Time Block Coded Spatial Modulation with Labeling Diversity

Application of labeling diversity to STBC-SM results in a system called STBC-SM scheme with labeling diversity (STBC-SM-LD) [11]. STBC-SM-LD achieves a better BER performance compared to the conventional Alamouti STBC-SM but maintains a similar structure to that of the conventional Alamouti STBC-SM system model [10]. However, a unique bit-to-constellation symbol mapper is employed for symbols transmitted in each of the two transmission slots. The selections of the antenna pairs for various antenna pair combinations remain unchanged as compared to [10]. Similarly, the ML detector also jointly estimates antenna pair index and symbol indices by performing an exhaustive search over all cM^2 possible antenna pair and symbol pair combinations [11]. Perfect channel estimation is assumed at the receiver. Furthermore, the

practical number of transmit antennas that can be used may also limit the STBC-SM-LD from achieving high bandwidth efficiencies.

1.2.2.3 Efficiency-Improved Alamouti Code

In the coherent scheme called efficiency-improved Alamouti (EI-Alamouti) code proposed by Ling and Li, multiple quadrature phase shift keying (QPSK) signal constellations are employed to improve the bandwidth efficiency of the Alamouti STBC [12]. For a single additional bit, two distinct QPSK constellations are employed. The second constellation is a rotated version of the conventional QPSK constellation. Symbols in each transmitted block are taken from the same constellation, therefore, the EI-Alamouti code preserves the full diversity of the conventional Alamouti STBC and allows the ML decoding for symbols to be decoupled at the receiver. The chosen constellation is a fixed function of the additional bit. The EI-Alamouti is a $2 \times N_{\mathrm{R}}$ system. A bit stream consisting of $d + 2\log_2 M$ random bits is fed into the EI-Alamouti transmitter to select a pair of Gray-coded MS symbols from one of the 2^d constellations for transmission. For $d = 1$, the additional bit 0 selects the conventional QPSK constellation denoted by A_1 in Figure 1-1, while bit 1 selects the rotated constellation denoted by A_2 in Figure 1-1.

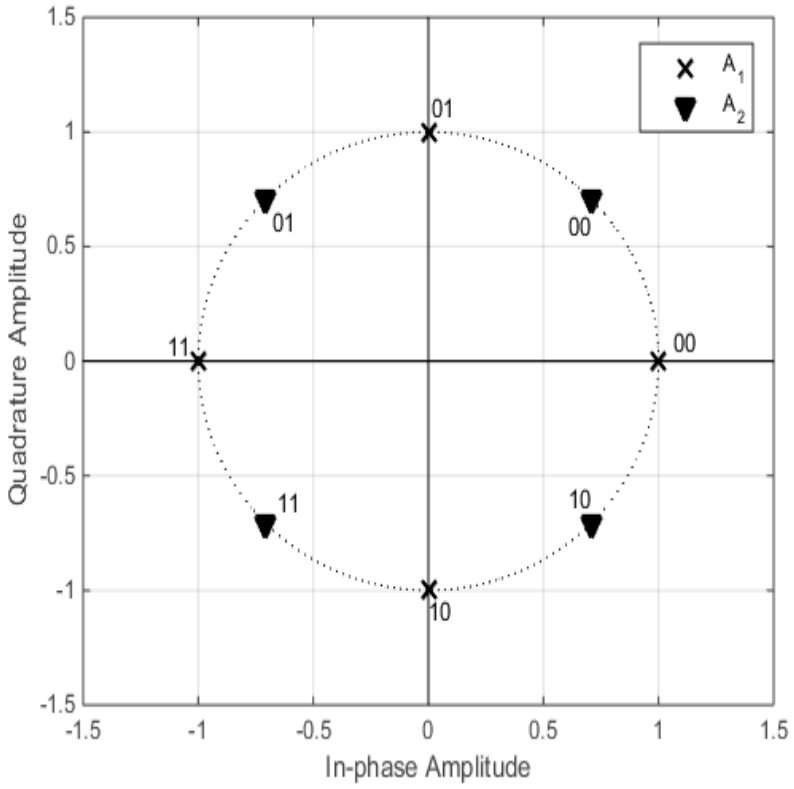

Figure 1-1: QPSK constellations for EI-Alamouti code [12]

The EI-Alamouti retains the Alamouti transmission matrix format, however, each transmission block contains one more information bit than in the conventional Alamouti system [12]. At the

receiver, the decision boundary method is employed to determine the additional bit, thereafter the ML decoding of the two MS symbols is decoupled. It is assumed that the channel state information (CSI) is available at the receiver. However, bandwidth efficiency is achieved at the expense of a degraded BER performance. The degraded error performance is due to the reduced effective minimum Euclidean distance between symbols caused by combining A_1 and A_2. The EI-Alamouti scheme has been extended to a four transmit antenna STBC [13].

1.2.2.4 Super-orthogonal Space-Time Block Code Using a Unitary Expansion

Super-orthogonal STBC improves the bandwidth efficiency and the error performance by expanding the orthogonal code via a unitary matrix transformation [8]. In unitary matrix transformation, the conventional orthogonal STBC is multiplied by several unitary matrices. Unitary matrix transformation does not expand the resulting modulation signal constellation, which prevents the undesirable increase of the peak-to-average power ratio (PAPR) of the transmitted M-QAM signal. The primary work of unitary matrix transformation is to increase the cardinality of the STBC set. The larger the STBC set is, the higher bandwidth efficiency can be achieved. To convey d additional bits per transmitted block requires a set with 2^d space-time signals. However, there are some design considerations that are taken into account in the design of employed unitary matrices. These include maintaining the PAPR of the conventional STBC, as well as maximizing parameters that govern the error performance of the STBC such as the minimum Euclidean distance to guarantee that the increased bandwidth efficiency does not degrade the error performance of the super-orthogonal code [8]. These design considerations put a restriction on the phase rotation and permutations that are allowed in the unitary matrices.

The impact of the super-orthogonal STBC has been the improvement in the bandwidth efficiency and BER performance of the STBC with four transmit antennas, since the availability of zeros in the space-time code with four transmit antennas is exploited in producing high-rate space-time codes with large Euclidean distances. However, the space-time code with two transmit antennas has a degrading error performance, which deteriorates further as the code rate is increased [8].

1.3 Literature Survey

In this section, we present the summary of the literature that leads to the development of trellis code-aided bandwidth efficiency improvement technique for differential Alamouti STBC transmitted over the Rayleigh frequency-flat fading channel and the extension of the trellis code-aided bandwidth efficiency improvement technique to USTLD.

1.3.1 Rayleigh Fading Channel

1.3.1.1 Wireless Multipath Fading Channels

In wireless channels, radio signals may go through reflection, absorption, diffraction and scattering by the objects between the source and the receiver [14]. As a result, signals reach the receiver via multiple independent paths and time instances. Therefore, each signal version experiences different delay, attenuation and phase shift while it is propagated from the source to the receiver. Signals arriving at the receiver from independent paths may result in destructive signal addition. This phenomenon is known as multipath fading propagation [14].

1.3.1.2 Rayleigh Fading Model

The Rayleigh fading channel is the specialised stochastic multipath fading when there is a lack of line-of-sight propagated signal, with a very large number of signal versions from independent paths arriving at the receiver [14]. In Rayleigh fading the amplitude gain is characterised by a distribution where the fading coefficient is expressed as:

$$h = h^I + \mathrm{j}h^Q \tag{1.1}$$

where h^I and h^Q are the in-phase and quadrature components, respectively, which are distributed as Gaussian random variables (RVs) with zero mean and variance of 0.5. The Rayleigh distributed fading amplitude α is given by [15]:

$$\alpha = \sqrt{|h^I|^2 + |h^Q|^2} \tag{1.2}$$

The probability density function (PDF) of the fading amplitude α is given by [15, Eq. 30]:

$$f_\alpha(\alpha) = \alpha \cdot \exp(-\alpha^2/2) \qquad \alpha \geq 0 \tag{1.3}$$

In this dissertation, all fading channels are assumed to be Rayleigh frequency-flat fading.

1.3.2 The Alamouti Space-time Block Coding System

Space-time block coding is a technique employed by wireless communication systems to mitigate the impairments of wireless multipath fading channels, and hence improve the link reliability. Space-time block coding exploits the independent fading nature of the several transmission paths between the source and the receiver by transmitting diverse versions of the information signals over multiple transmit antennas and multiple time slots, where there is high probability that some of the signals are less attenuated than others. Consequently, the received message signals are combined at the receiver in an optimal manner and hence, the overall link reliability is improved.

The first form of the STBC was introduced by Alamouti [2]. The Alamouti system is a $2 \times N_{\mathrm{R}}$ full-rate full-diversity system that transmits data by employing two transmit antennas and two

time slots. The modulated signal pair is transmitted over quasi-static multipath frequency-flat fading channels with additive white Gaussian noise (AWGN), where the fading coefficients are assumed to be constant over the pair of time slots but assume different values from one pair of time slots to another. It is assumed that the CSI is known at the receiver. The transmission matrix also known as the Alamouti STBC is defined as [2]:

$$\boldsymbol{X_A} = \begin{bmatrix} x_1 & x_2 \\ -x_2^* & x_1^* \end{bmatrix} \tag{1.4}$$

where symbols x_1 and x_2 belong to an M-QAM or M-PSK constellation. The rows of the matrix in (1.4) represent time slot 1 and time slot 2, respectively, the columns represent the transmit antenna 1 and transmit antenna 2, respectively, while the complex entries represent modulated signals (symbols) that are transmitted from each antenna during a given time slot. The Alamouti STBC is the only orthogonal full-rate STBC, such that $\boldsymbol{X_A}^H \boldsymbol{X_A} = (|x_1|^2 + |x_2|^2)\boldsymbol{I}_2$. The orthogonality property of the Alamouti STBC is exploited for LC linear decoding [2].

1.3.3 The Differential Alamouti Space-time Block Coding System

As discussed in Section 1.3.2, the coherent Alamouti STBC requires CSI to be available at the receiver. In order to estimate the CSI, the coherent system employs pilot (training) symbols, provided the change in channel conditions is slower than the baud [16]. However, rapid bursts of pilot symbols are required when channel conditions change quickly, thus increasing the channel estimation overhead. An increase in the channel estimation overhead increases the complexity at the receiver. Furthermore, rapid bursts of pilot symbols reduce the rate of transmission of information signals. Consequently, a noncoherent and differential scheme which eliminates the need for channel estimation would be desirable in fast changing channel conditions. Moreover, the elimination of channel estimation reduces the cost at the receiver [16].

Hwang et al developed an LC, noncoherent and differential STBC (DSTBC) system that uses M-QAM constellations [16]. The DSTBC system is an $N_\mathrm{T} \times N_\mathrm{R}$ system that transmits modulated signals (symbols) by employing a power normalised transmission matrix. The power normalisation factor is derived from the average power of previously transmitted symbols, and the purpose of power normalisation is to ensure that the transmission matrix peak power would not keep on increasing [3]. The differentially encoded signals are transmitted over quasi-static multipath frequency-flat fading channels with AWGN, where the fading coefficients are assumed to be constant over the pair of time slots but are different from one pair of time slots to another. In order to decode the received signals, the receiver requires the estimation of the fading channel's power, as well as the power normalisation factor that was employed at the transmitter. A DSTBC system developed by Xu et al, dubbed conventional differential detected-aided space-time block code (CDD-DSTBC), further eliminates the need for channel power estimation [3]. However,

CDD-DSTBC incurs an SNR penalty unless multiple symbol detection methods are employed [3]. The details of CDD-DSTBC are presented in Section 2.1.

1.3.4 The Uncoded Space-time Labeling Diversity System

Uncoded space-time labeling diversity (USTLD) is a recent two transmit antenna space-time block coded system proposed by Xu et al which achieves labeling diversity, and further achieves better error performance compared to the Alamouti STBC scheme [17]. USTLD achieves labeling diversity by mapping a block of data bits to symbols via two labeling maps. The USTLD system is a modification of the conventional Alamouti STBC system, where the fundamental idea is to transmit a mapped symbol pair in time slot 2 instead of the complex conjugates [11]. Compared to coded systems such as the bit-interleaved space-time coded modulation (BI-STCM) [18-20], USTLD has a lower decoding complexity and offers better energy efficiency [17]. Unlike the Alamouti STBC, the transmission matrix employed in the USTLD scheme is not orthogonal. Consequently, a higher detection complexity exists at the USTLD receiver since the employed ML detector performs an exhaustive joint symbol detection over all possible symbol pairs. The details of USTLD are presented in Section 2.2.

1.3.5 Orthogonal Projection Based LC Detection for Spatially Multiplexed Systems

An orthogonal projection (OP) based LC detection technique designed for spatially multiplexed systems has been employed to reduce the detection complexity at the USTLD receiver [11]. The fundamental principle of OP based LC detection is to independently estimate the most likely candidates of the transmitted symbols. Thereafter, conventional ML detection is employed to estimate the transmitted symbols from among the candidates. Therefore, the OP based detector significantly reduces the joint symbol detection search space for USTLD, since the ML detector only searches through the candidates. The details of the OP based LC detection scheme for USTLD are presented in Section 2.3.

1.3.6 Convolutional Coding and Decoding

In classical digital communication systems, a channel encoder that introduces redundant bits to the information bit stream is employed to improve noise immunity at the receiver. Redundant bits are used detect and correct errors in received information bits. One popular example of a channel encoder is known as a convolutional encoder. Generally, a convolutional encoder comprises of a shift register with a finite number of stages, where the outputs of the selected stages are added modulo-2 to generate encoded bits [21]. The convolutional encoder generates n bits for each accepted block of k information bits, where $n > k$. The redundant $n - k$ bits are a function of the k information bits as well as a span of preceding information bits [21]. Therefore, convolutional codes are specified as (n, k, L), where L is the constraint length. A convolutional encoder can be

described as a finite state machine with $2^{k(m-1)}$ states, where the state information is stored in memory registers and m is the number of memory registers [21].

A trellis diagram that shows the state transitions and the corresponding input and output bits can also be used to represent the convolutional encoder [21]. For that reason, the convolutional encoder is also be referred to as a trellis encoder. A convolutional encoder whose output bit stream retains the unaltered information bits in the first k positions is called a systematic convolutional encoder. In this dissertation, we employ systematic convolutional encoders to map additional bits to high-rate space-time signals.

Convolutional decoding employs a computationally efficient technique called the Viterbi algorithm (VA). The VA determines the most likely sequence of encoded information bits by finding the most probable path through a trellis [21]. The VA decoder computes a path metric for each path based on the received sequence, hence, the information bit sequence embedded in the path with the least path metric is detected as the correct information bit sequence.

1.3.7 The Trellis-coded Modulation Scheme

Trellis coded modulation (TCM) is a joint coding and modulation technique for digital transmission especially over bandlimited channels [22]. TCM schemes achieve coding gains over uncoded modulation schemes without the need to expand the bandwidth or reduce the effective information rate as required by traditional coding schemes such as convolutional coding discussed in Section 1.3.6. TCM employs a redundant modulation signal set in conjunction with a convolutional encoder to restrict the selection of modulating signals that can form coded sequences, therefore, if coded signal sequences are clearly separated in their Euclidean distances, then the transmitted coded signal sequences are most immune to channel disturbances [22]. To achieve large Euclidean distances between allowed coded signal sequences, TCM schemes expand the modulating signal alphabet to provide redundancy for trellis coding, and employ set partitioning (creation of signal subsets associated with each state transition) designed according to rules proposed by Ungerboeck [22].

In order to achieve coding gain, the maximized minimum Euclidean distance (free Euclidean distance) between coded sequences is designed to be significantly greater than the minimum distance between uncoded modulation signals under the same power, information rate and bandwidth conditions. In his work on TCM schemes, Ungerboeck observed that most of the achievable coding gain can be achieved by expanding signal sets used for uncoded modulation by a factor of two [22]. Therefore, if a signal set of size 2^k is used to transmit k bits in uncoded modulation, the corresponding TCM scheme would require an expanded signal set of size 2^n,

where $n = k + 1$. A typically example pair is the uncoded 4-PSK modulation scheme and the coded 8-PSK modulation scheme pair.

TCM schemes can be represented by trellis diagrams similar to those that describe the convolutional coding scheme, however, TCM trellis diagrams are labelled with redundant modulating signals rather than binary bits. Since TCM uses a convolutional encoder, a VA decoder is employed to recursively search for the most likely transmitted coded signal sequence. Decoding is performed in two major steps. The first step finds the signal closest to the received signal in Euclidean distance and stores the signal together with the associated Euclidean distance. The second step uses the previous accumulated Euclidean distances (path metrics) to find the most likely path through the trellis, hence, the coded signal sequence embedded in the path with the least overall path metric is detected as the transmitted sequence [23].

1.4 Motivation and Contributions

1.4.1 Proposed Trellis Code-aided Differential Space-time Block Code

Unitary matrix transformation is a technique employed to improve the bandwidth efficiency of STBC systems. However, work investigated in [8] exhibits a degrading BER performance as the bandwidth efficiency of a coherent Alamouti system is increased, while work in [24] focused only on coherent Alamouti systems using M-PSK. To the best of the author's knowledge, a more bandwidth efficient differential space-time block coded system that retains the BER performance of the conventional differential Alamouti scheme using M-QAM has not been reported in the literature.

Based on the above motivation, the contributions are:

Trellis code-aided bandwidth efficiency improvement technique for space-time block coded wireless communication systems is investigated and developed, and a high rate differential space-time block coded system called trellis code-aided DSTBC (TC-DSTBC) is proposed. Moreover, the TC-DSTBC system is shown to retain the BER performance of the conventional differential Alamouti system under the same channel and AWGN conditions.

1.4.2 Proposed Enhanced Uncoded Space-time Labeling Diversity

Since TC-DSTBC retains the BER performance of the conventional differential Alamouti system with improvement in bandwidth efficiency; this motivated for an extension of the trellis code-aided bandwidth efficiency improvement technique to USTLD.

Based on the above motivation, the contributions are:

1. A new system is proposed where, the trellis code-aided bandwidth efficiency improvement technique is applied to USTLD; the proposed system is referred to as E-USTLD. E-USTLD exploits the advantages of both high bandwidth efficiency and labeling diversity. We further show that E-USTLD retains BER performance of the conventional USTLD system under the same channel and AWGN conditions for various square M-QAM modulation orders such as 16-QAM and 64-QAM.

2. A closed-form lower bound on the average bit error probability (BEP) for E-USTLD employing square M-QAM over i.i.d. Rayleigh frequency-flat fading channels is derived.

1.4.3 Orthogonal Projection Based Viterbi Algorithm Detection Scheme

Optimal BER performance of TC-STBC and E-USTLD is achieved via the Viterbi algorithm based detector that employs ML estimation processes. Consequently, there is high computational complexity at the receiver that reduces the power efficiency and also poses receiver hardware implementation challenges. This motivates for OP based LC detection scheme developed for USTLD [11] to be extended to E-USTLD.

Based on the above motivation, the contributions are:

1. E-USTLD Viterbi algorithm (VA) detection scheme that implements OP based near-ML detection is proposed.

2. We further show that the E-USTLD system with a VA-based detection scheme that implements LC near-ML detection attains near-optimal BER performance.

1.5 Structure of this Dissertation

Chapter 2 firstly, presents the background and system model for the conventional differential detection-aided differential STBC (CDD-DSTBC) using M-QAM, and thereafter, presents the simulation results for the CDD-DSTBC system and compares these results with simulation and analytical results of the coherent Alamouti STBC. Secondly, Chapter 2 presents the background and system model for the USTLD system together with the analytical bounds for the average BER over Rayleigh frequency-flat fading channels. Thereafter, presents the simulation and analytical results for the USTLD system. Lastly, Chapter 2 presents the OP based LC near-ML detection scheme for USTLD.

Chapter 3 presents the trellis code-aided bandwidth efficiency improvement technique and the trellis code-aided DSTBC (TC-DSTBC) system. Thereafter, Chapter 3 presents the numerical results of the TC-DSTBC system and compares these results with the CDD-DSTBC system as well as with the coherent Alamouti STBC system under the same i.i.d. Rayleigh frequency-flat fading channel and AWGN conditions.

Chapter 4 extends the trellis code-aided bandwidth efficiency improvement technique to the USTLD system where a new system referred to as enhanced USTLD (E-USTLD) is proposed. Chapter 4 also derives the analytical bound for the average BER performance over i.i.d. Rayleigh frequency-flat fading channels. Thereafter, Chapter 4 presents numerical and analytical results for E-USTLD and compares these results with the USTLD system under the same the same i.i.d. Rayleigh frequency-flat fading channel and AWGN conditions.

Chapter 5 extends the OP based LC near-ML detection scheme to the E-USTLD detector.

Chapter 6 presents a summary of research contributions, briefly suggests future research avenues and finally draws concluding remarks.

2. Background and System Models

In this chapter we present the background work and system models that are of paramount importance to the work that is presented in chapters that follow.

2.1 Conventional Differential Detected-aided Alamouti Space-time Block Code

2.1.1 System Model

The conventional differential detected-aided Alamouti space-time block coding system (referred to as CDD-DSTBC) is an $N_{\mathrm{T}} \times N_{\mathrm{R}}$ system with $N_{\mathrm{T}} = 2$ as depicted in Figure 2-1 [3].

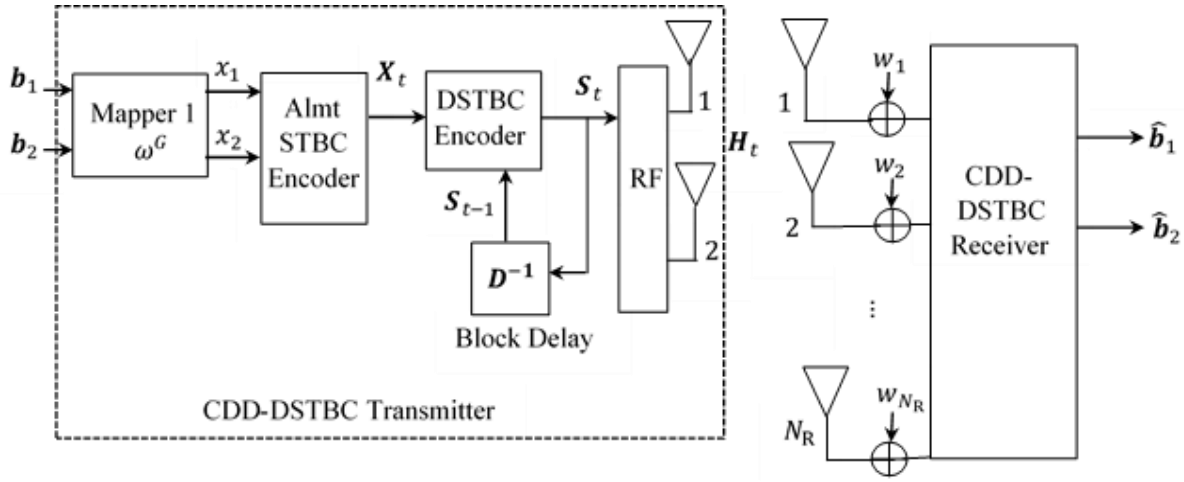

Figure 2-1: Conventional Differential Detected-Aided Alamouti Space-time Block Coding System

The transmission is initialised by sending the STBC $\boldsymbol{S}_0$ that consists of arbitrary symbols as shown in (2.1).

$$\boldsymbol{S}_0 = \begin{bmatrix} s_0^1 & s_0^2 \\ -s_0^{2^*} & s_0^{1^*} \end{bmatrix} \tag{2.1}$$

At time slot 1, symbols s_0^1, s_0^2, and at time slot 2, symbols $-s_0^{2^*}$, $s_0^{1^*}$ are respectively, transmitted from transmit antenna 1 and 2. Thereafter, at each time instant t, a bit stream that consists of $2\log_2 M$ random bits $\boldsymbol{b} = [\boldsymbol{b_1} \quad \boldsymbol{b_2}]$ is fed into Mapper 1 (ω^G), where $\boldsymbol{b}_1 = [b_{1,1}\ b_{1,2}\ \cdots\ b_{1,m}]$ and $\boldsymbol{b}_2 = [b_{2,1}\ b_{2,2}\ \cdots\ b_{2,m}]$ and $m = \log_2 M$. Mapper 1 employs the Gray-coded labeling map shown in Appendix B to respectively, map $\boldsymbol{b}_1$ and $\boldsymbol{b}_2$ onto M-QAM modulated symbols x_t^1 and x_t^2. Symbols x_t^1 and x_t^2 are normalised such that $E\{|x_t^1|^2\} = E\{|x_t^2|^2\} = 1$. The two symbols are then fed into the Alamouti STBC encoder, and yield the STBC $\boldsymbol{X}_t$, given by:

$$\boldsymbol{X}_t = \begin{bmatrix} x_t^1 & x_t^2 \\ -x_t^{2^*} & x_t^{1^*} \end{bmatrix} \tag{2.2}$$

Prior to transmission, $\boldsymbol{X}_t$ undergoes a differential encoding process that is defined as [3, Eq. (1)]:

$$\boldsymbol{S}_t = (\beta_{t-1})^{-1}\boldsymbol{X}_t\boldsymbol{S}_{t-1} \tag{2.3}$$

where $\boldsymbol{S}_{t-1}$ is the DSTBC transmitted at the time instant prior to t. The power normalisation factor $(\beta_{t-1})^{-1}$ defined by $\beta_{t-1} = \sqrt{|s_{t-1}^1|^2 + |s_{t-1}^2|^2}$ prevents an increase of the transmission matrix peak power. $\boldsymbol{S}_t$ is transmitted over an $2 \times N_{\mathrm{R}}$ quasi-static Rayleigh frequency-flat fading channel with $2 \times N_{\mathrm{R}}$ dimensional AWGN, where the channel gains are assumed to be constant over the pair of time slots and remain constant for the duration of transmitting $N + 1$ DSTBCs.

The $2 \times N_{\mathrm{R}}$ t^{th} received signal matrix is expressed as:

$$\boldsymbol{Y}_t = \sqrt{\rho/2}\,\boldsymbol{S}_t\boldsymbol{H}_t + \boldsymbol{W}_t \tag{2.4}$$

where $\rho/2$ is the average SNR at each receive antenna, $\boldsymbol{H}_t$ is the $2 \times N_{\mathrm{R}}$ channel matrix and $\boldsymbol{W}_t$ is the $2 \times N_{\mathrm{R}}$ AWGN matrix. The complex entries of both $\boldsymbol{H}_t$ and $\boldsymbol{W}_t$ are i.i.d. Gaussian RVs distributed as $CN(0,1)$. Equation (2.4) may be further expressed as [3, Eqn. (5)]:

$$\boldsymbol{Y}_t = (\beta_{t-1})^{-1}\boldsymbol{X}_t(\boldsymbol{Y}_{t-1} - \boldsymbol{W}_{t-1}) + \boldsymbol{W}_t \tag{2.5}$$

Therefore, transmitted symbols are estimated based on minimising the following ML metric:

$$[\hat{x}_t^1 \quad \hat{x}_t^2] = \underset{\widehat{\boldsymbol{X}}_t \in \boldsymbol{\chi_A}}{\operatorname{argmin}} \left\| \boldsymbol{Y}_t - (\beta_{t-1})^{-1}\widehat{\boldsymbol{X}}_t\boldsymbol{Y}_{t-1} \right\|_F^2 \tag{2.6}$$

where $\boldsymbol{\chi_A}$ is the codebook that contains all the M^2 distinct Alamouti codewords.

2.1.2 BER Performance of the Coherent Alamouti System

The average BER performance of the coherent Alamouti STBC is estimated by the closed form expression given by [25, eqn. (19)]:

$$P_{BER}(e) = \frac{a}{nm}\left\{\frac{1}{2}\left(\frac{2}{b\bar{\gamma}+2}\right)^{N_{\mathrm{R}}} - \frac{a}{2}\left(\frac{1}{b\bar{\gamma}+1}\right)^{N_{\mathrm{R}}} + (1-a)\sum_{i=1}^{n-1}\left(\frac{S_i}{b\bar{\gamma}+S_i}\right)^{N_R} + \sum_{i=n}^{2n-1}\left(\frac{S_i}{b\bar{\gamma}+S_i}\right)^{N_R}\right\} \tag{2.7}$$

where $S_i = 2\sin^2\frac{i\pi}{4n}$, $a = 4\left(1 - \frac{1}{\sqrt{M}}\right)$, $b = 4\left(1 - \frac{1}{\sqrt{M}}\right)^2$, $\bar{\gamma} = \rho/2$ is the average SNR at each receive antenna and n is the number of iterations for convergence ($n > 10$) [25].

2.1.3 Simulation and Analytical Results

In this section the simulation results for $2 \times N_{\mathrm{R}}$ CDD-DSTBC and $2 \times N_{\mathrm{R}}$ coherent Alamouti system together with analytical results for the coherent Alamouti system over i.i.d. Rayleigh frequency-flat fading channels are presented and compared for the following modulation schemes:

1. 16-QAM

2. 64-QAM

The average BER of the coherent Alamouti system given by evaluating the closed form expression in (2.7). The simulation results for the coherent Alamouti STBC are given by the model presented in [2]. Furthermore, Monte Carlo simulations were performed, where the average BER is plotted against the average SNR. All BER performance comparisons are made at a BER value of 10^{-5}. For simulation purposes, the fading channel and noise parameters were defined in line with those presented in (2.4) of Section 2.1.1. We also assumed that $N_R = 4$; the CSI is not known at the receiver; there is sufficient separation of transmit antennas such that all channel gains are independent of each other; MRC reception is employed.

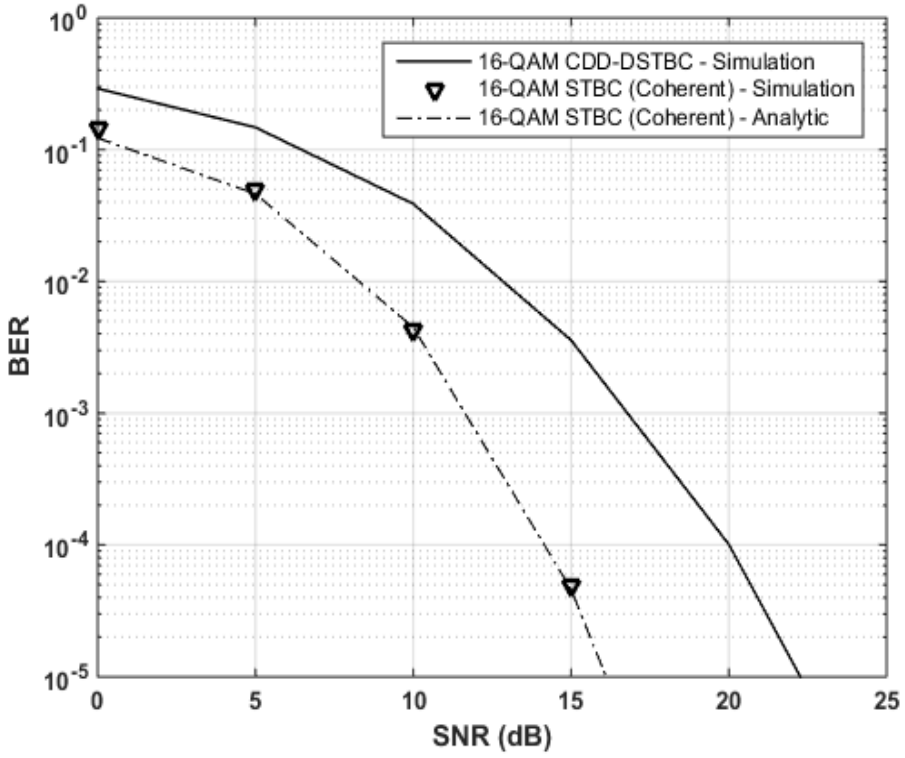

Figure 2-2: BER performance of the CDD-DSTBC in comparison to coherent Alamouti system for 16-QAM.

It can be observed from Figure 2-2 that there is a performance gap of approximately 5dB between the coherent Alamouti STBC and CDD-DSTBC with 16QAM, which is similar to the SNR gap shown in [3, Fig. 1(a)]. The performance gap is much higher than the 3dB performance gap reported for DSTBC with MPSK [4]. As with the SNR gap shown in [3, Fig. 1(a)], the SNR gap increases with an increase in M-QAM modulation order. In Figure 2-3, the SNR gap between the coherent Alamouti STBC and CDD-DSTBC with 64QAM exceeds 5dB at high SNR.

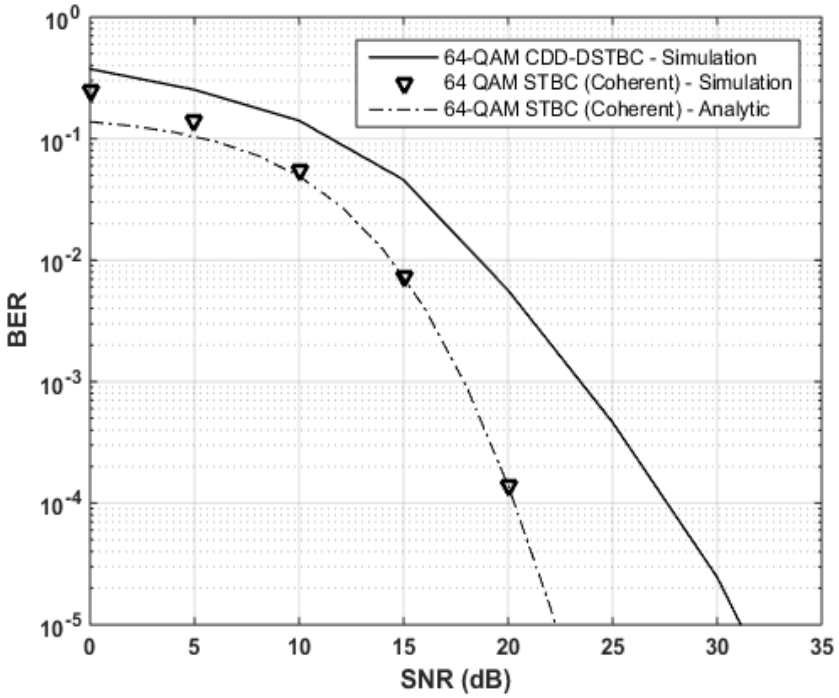

Figure 2-3: BER performance of the CDD-DSTBC in comparison to coherent Alamouti system for 64-QAM.

In the next section the detailed USTLD system is presented.

2.2 Uncoded Space-time Labeling Diversity

2.2.1 System Model

The space-time labeling diversity for uncoded systems (referred to as USTLD) is a $2 \times N_{\mathrm{R}}$ system [17]. A bit stream that consists of $2\log_2 M$ random bits $\boldsymbol{b} = [\boldsymbol{b}_1 \quad \boldsymbol{b}_2]$ is fed into two mappers, Mapper 1 (ω^G) that employs the Gray-coded labeling map and Mapper 2 (ω^O) that employs the optimized labeling map [2], with each mapper yielding two modulated M-QAM symbol pairs $\boldsymbol{x}_1 = \left[x_q^1 \; x_r^2\right]^T$ and $\boldsymbol{x}_2 = \left[\bar{x}_r^2 \; \bar{x}_q^1\right]^T$ for transmission in the first and second time slots, respectively, where $q, r \in [1\!:\!M]$, $\boldsymbol{b}_1 = [b_{1,1}\, b_{1,2} \cdots b_{1,m}]$, $\boldsymbol{b}_2 = [b_{2,1}\, b_{2,2} \cdots b_{2,m}]$, $E\left\{\left|x_q^1\right|^2\right\} = E\{|x_r^2|^2\} = E\{|\bar{x}_r^2|^2\} = E\left\{\left|\bar{x}_q^1\right|^2\right\} = 1$, and $m = \log_2 M$. The symbol labels are expressed as $q = 1 + \sum_{k=1}^{m} b_{1,k} 2^{m-k}$ and $r = 1 + \sum_{k=1}^{m} b_{2,k} 2^{m-k}$. Xu et al defined $\boldsymbol{\chi}$ as a set that contains all the possible modulated symbol pairs $(\boldsymbol{x}_1, \boldsymbol{x}_2)$, such that $(\boldsymbol{x}_1, \boldsymbol{x}_2) \in \boldsymbol{\chi}$. The $N_R \times 1$ received signal vector for the t^{th} time slot is expressed as [17]:

$$\boldsymbol{y}_t = \sqrt{\rho/2}\, \boldsymbol{H}_t \boldsymbol{x}_t + \boldsymbol{\eta}_t \qquad t \in [1\!:\!2] \tag{2.8}$$

where $\rho/2$ is the average SNR at each receive antenna, $\boldsymbol{\eta}_t = \left[\eta_{1,t}\, \eta_{2,t} \cdots \eta_{N_R,t}\right]^T$ is the $N_R \times 1$ AWGN vector, $\boldsymbol{H}_t$ is the $N_R \times 2$ channel matrix modelled as a frequency-flat Rayleigh fading channel, where the channel gains remain constant during a time slot but assume independent values from one time slot to another with $\boldsymbol{H}_t = [\boldsymbol{h}_1^t\, \boldsymbol{h}_2^t]$ and $\boldsymbol{h}_i^t = \left[h_{1,i}^t\, h_{2,i}^t \cdots h_{N_R,i}^t\right]^T$, $i \in [1{:}\,2]$. The entries of $\boldsymbol{H}_t$ and $\boldsymbol{\eta}_t$ are i.i.d. complex Gaussian RVs distributed as $CN(0,1)$.

Therefore, the receiver estimates the transmitted symbols by minimising the ML metric in (2.9):

$$\left[x_{\hat{q}}^1\, x_{\hat{r}}^2\right] = \underset{(\boldsymbol{x}_1,\boldsymbol{x}_2)\in\boldsymbol{\chi}}{\operatorname{argmin}} \left(\sum_{t=1}^{2} \left\|\boldsymbol{y}_t - \sqrt{\rho/2}\, \boldsymbol{H}_t \boldsymbol{x}_t\right\|_F^2\right) \tag{2.9}$$

2.2.2 Analytical Bound for USTLD

A closed-form lower bound for USTLD over an i.i.d. Rayleigh frequency-flat fading channel was presented in [17]. The expression is based on the assumption that at high SNR one transmitted symbol pair, $(x_r^2\ \ \bar{x}_r^2)$, is estimated correctly while the other transmitted symbol pair, $\left(x_q^1\ \bar{x}_q^1\right)$, is estimated with errors. The closed form expression is given as [17]:

$$P_{BER}(e) = \frac{1}{mM} \sum_{q=1}^{M} \sum_{\hat{q}\neq q}^{M} N_{\hat{q},q}\, \frac{1}{2n} \left[\frac{1}{2}\left(\frac{8}{\rho d_1 + 8}\right)^{N_R} \left(\frac{8}{\rho d_2 + 8}\right)^{N_R} + \sum_{i=1}^{n-1} \left(\frac{8S_i}{\rho d_1 + 8S_i}\right)^{N_R} \left(\frac{8S_i}{\rho d_2 + 8S_i}\right)^{N_R}\right] \tag{2.10}$$

where $N_{\hat{q},q}$ is the number of bit errors between symbols x_q^1 and $x_{\hat{q}}^1$, $S_i = 2\sin^2\frac{i\pi}{2n}$, $d_1 = \left|x_{\hat{q}}^1 - x_q^1\right|^2$, $d_2 = \left|\bar{x}_{\hat{q}}^1 - \bar{x}_q^1\right|^2$ and $n > 10$.

2.2.3 Simulation and Analytical Results

In this section the simulation and analytical results for the $2 \times N_R$ USTLD system over i.i.d. Rayleigh frequency-flat fading channels are presented and compared for the following modulation schemes:

1. 16-QAM

2. 64-QAM

Monte Carlo simulations were performed, where the average BER is plotted against the average SNR. All BER performance comparisons are made at a BER value of 10^{-6}. For simulation purposes, the fading channel and noise parameters were defined in line with those presented in (2.8) of Section 2.2.1. Labeling maps are as illustrated in Govindasamy et al [11] (see Appendix B). We also assumed that $N_R = 4$; channel is fully known at the receiver; all channel gains remain constant during a time slot but assume independent values from one time slot to another; MRC reception is employed.

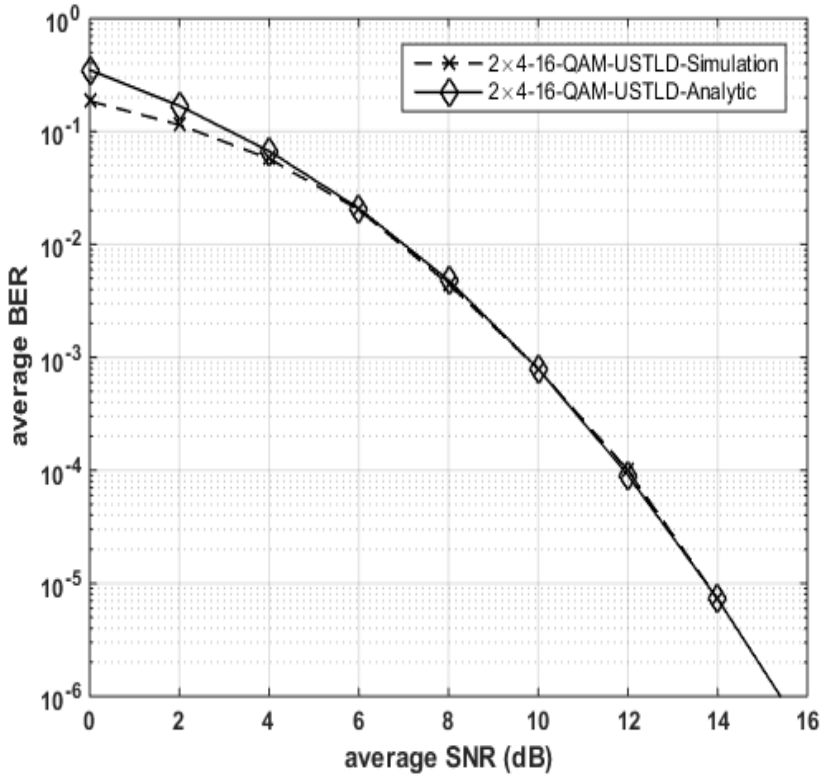

Figure 2-4: BER performance of the USTLD system for 16-QAM with analytic bounds.

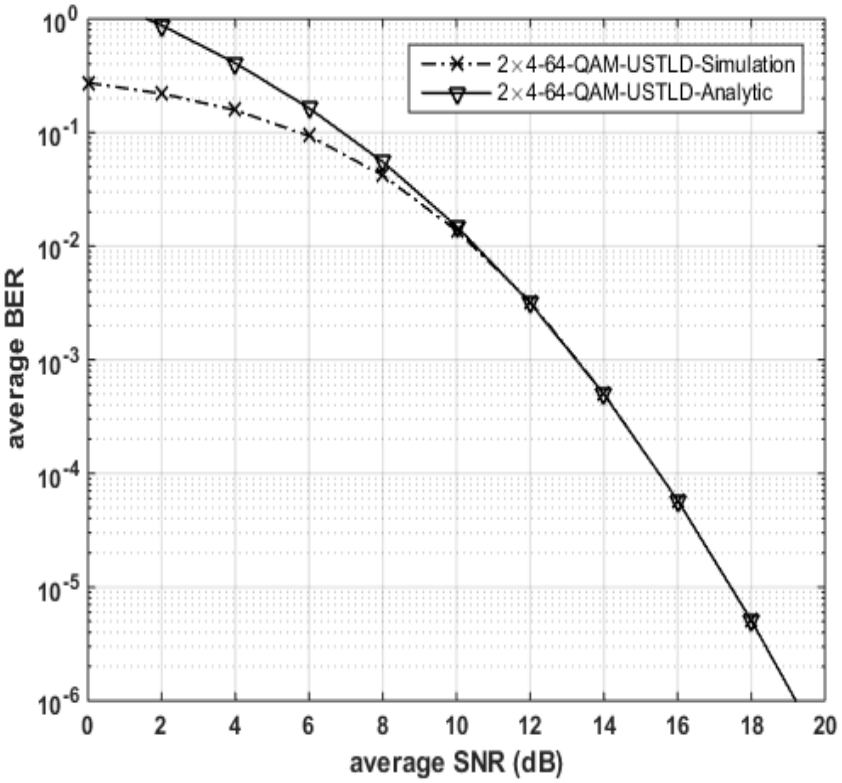

Figure 2-5: BER performance of the USTLD system for 64-QAM with analytic bounds.

Simulation and analytical results for USTLD with 16-QAM and 64-QAM are presented in figure 2-4 and Figure 2-5, respectively. It can be observed that, in all cases, the analytical results converge to the Monte Carlo simulation results.

2.3 Orthogonal Projection Based Low-Complexity detection scheme for USTLD

In this section the OP based LC near-ML detection scheme for USTLD is presented [11]. Firstly, (2.8) is expanded as:

$$\boldsymbol{y}_1 = \sqrt{\rho/2}\,\boldsymbol{h}_1^1 x_q^1 + \sqrt{\rho/2}\,\boldsymbol{h}_2^1 x_r^2 + \boldsymbol{\eta}_1 \tag{2.11}$$

$$\boldsymbol{y}_2 = \sqrt{\rho/2}\,\boldsymbol{h}_1^2 \bar{x}_r^2 + \sqrt{\rho/2}\,\boldsymbol{h}_2^2 \bar{x}_q^1 + \boldsymbol{\eta}_2 \tag{2.12}$$

Thereafter, projection matrices $\boldsymbol{P}_i^t, \quad i,t \in [1:2]$ which, respectively, project a signal on the subspace orthogonal to $\boldsymbol{h}_i^t$ such that $\boldsymbol{P}_i^t \boldsymbol{h}_i^t = 0$ are defined. The projection matrices $\boldsymbol{P}_i^t$ are given by [11]:

$$\boldsymbol{P}_i^t = I_{N_\mathrm{R}} - \boldsymbol{h}_i^t \left(\left(\boldsymbol{h}_i^t\right)^H \boldsymbol{h}_i^t \right)^{-1} \left(\boldsymbol{h}_i^t\right)^H \tag{2.13}$$

This is followed by the computation of the projection subspaces $\boldsymbol{r}_{t,q}^i, \boldsymbol{r}_{t,r}^i \in \boldsymbol{\mathcal{R}}$ as [11]:

$$\boldsymbol{r}_{1,q}^1 = \boldsymbol{y}_1 - \sqrt{\rho/2}\,\boldsymbol{h}_1^1 x_q^1 \tag{2.14}$$

$$\boldsymbol{r}_{2,r}^1 = \boldsymbol{y}_1 - \sqrt{\rho/2}\,\boldsymbol{h}_2^1 x_r^2 \tag{2.15}$$

$$\boldsymbol{r}_{1,r}^2 = \boldsymbol{y}_2 - \sqrt{\rho/2}\,\boldsymbol{h}_1^2 \bar{x}_r^2 \tag{2.16}$$

$$\boldsymbol{r}_{2,q}^2 = \boldsymbol{y}_2 - \sqrt{\rho/2}\,\boldsymbol{h}_2^2 \bar{x}_q^1 \tag{2.17}$$

where $\boldsymbol{\mathcal{R}}$ is the set of all computed projection subspaces.

Let λ be a mapper that acts on M-QAM symbols according to the mapping rule proposed by Xu et al [17], such that $\lambda\left(x_q^1\right) = \bar{x}_q^1$ and $\lambda(x_r^2) = \bar{x}_r^2$. Then $x_q^1, x_r^2 \in \boldsymbol{\Omega}_M$ and $\bar{x}_q^1, \bar{x}_r^2 \in \lambda(\boldsymbol{\Omega}_M)$. In order to respectively, estimate l_1 and l_2 most likely candidates for x_q^1 and x_r^2, candidate symbols with the smallest projection norms according to (2.18) and (2.19) are chosen. Note, optimal values of l_1 and l_2 are determined such that $l_1 l_2 < M^2$. In [11], a 60.2% reduction in detection complexity was achieved using $l_1 = 8$ and $l_2 = 6$ for USTLD using 16-QAM.

$$\hat{x}_q^1 = \underset{\boldsymbol{r}_{1,q}^1 \; \boldsymbol{r}_{2,q}^2 \in \boldsymbol{\mathcal{R}}}{\operatorname{argmin}} \left\| \boldsymbol{P}_2^1 \boldsymbol{r}_{1,q}^1 + \boldsymbol{P}_1^2\, \boldsymbol{r}_{2,q}^2 \right\|_F^2 \quad q \in [1:M] \tag{2.18}$$

$$\hat{x}_r^2 = \underset{\boldsymbol{r}_{2,r}^1 \; \boldsymbol{r}_{1,r}^2 \in \boldsymbol{\mathcal{R}}}{\operatorname{argmin}} \left\| \boldsymbol{P}_1^1 \boldsymbol{r}_{2,r}^1 + \boldsymbol{P}_2^2\, \boldsymbol{r}_{1,r}^2 \right\|_F^2 \quad r \in [1:M] \tag{2.19}$$

The chosen most likely candidates for x_q^1 and x_r^2 are stored in candidate sets $\boldsymbol{z}_q$ and $\boldsymbol{z}_r$, respectively. Finally, the transmitted symbols are estimated by performing an ML search through the elements of the candidate sets $\boldsymbol{z}_q$ and $\boldsymbol{z}_r$. The estimation process is based on minimising the following ML metric:

$$\left[x_{\hat{q}}^1\ x_{\hat{r}}^2\right] = \underset{\substack{x_{\hat{q},n_1}^1, x_{\hat{r},n_2}^2 \\ \bar{x}_{\hat{q},n_1}^1, \bar{x}_{\hat{r},n_2}^2}}{\operatorname{argmin}} \left\{ \begin{matrix} \left\| \boldsymbol{y}_1 - \sqrt{\rho/2}\, \boldsymbol{h}_1^1 x_{\hat{q},n_1}^1 - \sqrt{\rho/2}\, \boldsymbol{h}_2^1 x_{\hat{r},n_2}^2 \right\|_F^2 \\ + \left\| \boldsymbol{y}_2 - \sqrt{\rho/2}\, \boldsymbol{h}_1^2 \bar{x}_{\hat{r},n_2}^2 - \sqrt{\rho/2}\, \boldsymbol{h}_2^2 \bar{x}_{\hat{q},n_1}^1 \right\|_F^2 \end{matrix} \right\} \tag{2.20}$$

where $x_{\hat{q},n_1}^1 \in \boldsymbol{z}_q$, $x_{\hat{r},n_2}^2 \in \boldsymbol{z}_r$, $x_{\hat{q},n_1}^1 \in \lambda(\boldsymbol{z}_q)$, $x_{\hat{r},n_2}^2 \in \lambda(\boldsymbol{z}_r)$, $n_1 \in [1{:}\, l_1]$, $n_2 \in [1{:}\, l_2]$.

In this dissertation, the LC near-ML detection scheme for USTLD is extended to the more bandwidth efficient E-USTLD system as presented in Chapter 5. In the next chapter, the TC-DSTBC system is presented and compared with the CDD-DSTBC and the coherent Alamouti systems under the same fading channel and AWGN conditions.

3. Trellis Code-aided Differential Space-time Block Code

This chapter develops the technique for enhancing the bandwidth efficiency for space-time block coded wireless communication systems and presents the mathematical model of the high-rate differentially transmitted Alamouti system. The bandwidth efficiency improvement technique increases the bit-rate of the Alamouti STBC by superimposing additional bits onto the expanded Alamouti STBC. The new high-rate differential Alamouti system is presented in the form of a system called trellis code-aided DSTBC (TC-DSTBC).

3.1 Bandwidth Efficiency Improvement Technique

In this section, we present the technique for enhancing the bandwidth efficiency of the STBC with $N_{\mathrm{T}} = 2$. Firstly, we expand the conventional Alamouti STBC via unitary matrix transformation [8]. Thereafter, we incorporate trellis coding into the mapping of additional bits to the expanded STBC to improve the bandwidth efficiency.

3.1.1 STBC Expansion

Unitary matrix transformation is employed in expanding the conventional Alamouti STBC so as to introduce redundancy that is required for trellis coding. The Alamouti code $\boldsymbol{X_A}$ in (1.4) of Section 1.3.2 is multiplied by diagonal unitary matrices. Unitary matrix transformation does not increase the size of the resulting M-QAM symbol set, thus preventing an increase of the PAPR of the transmitted symbol [8]. A total of 2^{d+1} diagonal unitary matrices is required in order to send d additional bits per space-time codeword. Employing 2^{d+1} unitary matrices ensures that the trellis code-aided scheme has STBCs (distinct transmission matrices) of twice the cardinality when compared to schemes with unaided mapping, thus satisfying the redundancy requirement for trellis coding [23]. Diagonal unitary matrices of the form shown in (3.1) are employed.

$$\boldsymbol{U} = \begin{bmatrix} \mathrm{e}^{j\theta_1} & 0 \\ 0 & \mathrm{e}^{j\theta_2} \end{bmatrix} \quad 0 \leq \theta_i < 2\pi, i \in [1{:}\,2] \tag{3.1}$$

where θ_1 and θ_2 are variable rotational angles. While a computer-aided numerical search can be used to find 2^{d+1} combinations of θ_1 and θ_2, which give a set of unitary matrices with the optimal Euclidean distance distribution [8], the same can be found by searching the literature. The literature search reveals that the optimal Euclidean distribution can be realized by maintaining $\theta_1 = 0$, while varying the θ_2 in equal steps over the entire 2π range or vice versa [8,26]. For conventionality purposes, $\theta_1 = 0$ is used in this dissertation. Therefore, unitary matrices of the form shown in (3.2) are employed in the STBC expansion.

$$\boldsymbol{U}_k = \begin{bmatrix} 1 & 0 \\ 0 & \mathrm{e}^{j\theta_k} \end{bmatrix} k \in \mathbb{Z}_{\geq 0} \tag{3.2}$$

where $\theta_k = 2\pi k/2^{d+1}$, for all $k \in [0: 2^{d+1} - 1]$, is the rotational angle. High-rate STBCs are then formulated from (1.4) and (3.2) as $\boldsymbol{B}_k = \boldsymbol{X_A U}_k$. In expanded form, the high-rate STBCs are expressed as:

$$\boldsymbol{B}_k = \begin{bmatrix} x_1 & x_2 \mathrm{e}^{j\theta_k} \\ -x_2^* & x_1^* \mathrm{e}^{j\theta_k} \end{bmatrix}, k \in [0: 2^{d+1} - 1] \tag{3.3}$$

where the rotational angle θ_k encodes additional bits. It is assumed that each codebook denoted by $\boldsymbol{\chi}_k$ contains M^2 distinct codewords of the high-rate STBC $\boldsymbol{B}_k$, $k \in [0: 2^{d+1} - 1]$, since there are M^2 possible combinations of symbols x_1 and x_2. M is the modulation order. For example, $\boldsymbol{\chi}_0$ contains M^2 distinct codewords of type $\boldsymbol{B}_0$, which have the same rotational angle $\theta_0 = 0$. Table 3.1 shows values of rotational angles corresponding to all high-rate STBCs of (3.3) for both $d = 1$ and $d = 2$.

Table 3-1: High-rate STBCs and corresponding rotational angles

High-rate STBC	$d = 1$	$d = 2$
$\boldsymbol{B}_0$	$\theta_0 = 0$	$\theta_0 = 0$
$\boldsymbol{B}_1$	$\theta_1 = \frac{\pi}{2}$	$\theta_1 = \frac{\pi}{4}$
$\boldsymbol{B}_2$	$\theta_2 = \pi$	$\theta_2 = \frac{\pi}{2}$
$\boldsymbol{B}_3$	$\theta_3 = \frac{3\pi}{2}$	$\theta_3 = \frac{3\pi}{4}$
$\boldsymbol{B}_4$		$\theta_4 = \pi$
$\boldsymbol{B}_5$		$\theta_5 = \frac{5\pi}{4}$
$\boldsymbol{B}_6$		$\theta_6 = \frac{3\pi}{2}$
$\boldsymbol{B}_7$		$\theta_7 = \frac{7\pi}{4}$

Space-time codes in adjacent rows of Table 3.1 are at the minimum maximised squared Frobenius distance from each other. For each value of d, the STBCs $\boldsymbol{B}_0$ and $\boldsymbol{B}_{2^{d+1}-1}$ are considered to be in adjacent rows. The downside of the expanded STBC is the loss of diversity as revealed by the analysis in Section 3.1.2.

3.1.2 Analysis of Diversity

In the TC-DSTBC system, all codebooks denoted by $\boldsymbol{\chi}_k$, $k \in [0: 2^{d+1} - 1]$, are considered as belonging to a larger codebook $\boldsymbol{\chi}$. For full diversity to be preserved, a full rank codeword difference matrix must exist between any two distinct codewords from $\boldsymbol{\chi}$ [27]. Consider $\boldsymbol{X}_i, \boldsymbol{X}_l \in \boldsymbol{\chi}$ where $\boldsymbol{X}_i \in \boldsymbol{\chi}_0$ and $\boldsymbol{X}_l \in \boldsymbol{\chi}_1$. Assuming that the same symbols are used in the two distinct

codewords i.e. $x_n = x_1 = x_2$, the codeword difference matrix $\boldsymbol{X}_{diff}$ would be given accordingly as:

$$\boldsymbol{X}_{diff} = \begin{bmatrix} 0 & x_n(1 - \mathrm{e}^{j\theta_1}) \\ 0 & x_n^*(1 - \mathrm{e}^{j\theta_1}) \end{bmatrix} \tag{3.4}$$

The resulting codeword difference matrix has a rank of one. This implies that diversity is sacrificed in the high-rate STBCs of (3.3), hence, the error performance of the high-rate STBC is likely to be degraded unless interventions to counteract the error performance degradation are made.

3.1.3 Trellis Code-aided Mapping of Additional Bits to High-rate STBCs

In this section, we incorporate trellis coding in the mapping of additional bits to high-rate STBCs to counteract the undesirable effect of loss of diversity in the form of error performance degradation. Trellis coding maximises the sum of squared Frobenius distances between possible sequences of transmitted high-rate codewords to boost the error performance of the high-rate STBC. The sum of squared Frobenius distances between sequences of high-rate codewords is maximized by ensuring that codewords associated with trellis state transitions that originate from or merge into the same trellis state are maximally apart. In this dissertation, the $d/d+1$-rate 2^{d+1}-state systematic trellis encoder of [23] is employed in the mapping of additional bits to the high-rate STBC. Systematic trellis encoders of [23, Fig. 17] and [23, Fig. 3] are respectively, employed for $d = 1$ and $d = 2$. The employed trellis encoders associate each trellis path with a single high-rate STBC of (3.3). Consequently, the trellis diagrams of Figure 3-1 and Figure 3-2 are respectively, employed in the mapping of additional bits for $d = 1$ and $d = 2$.

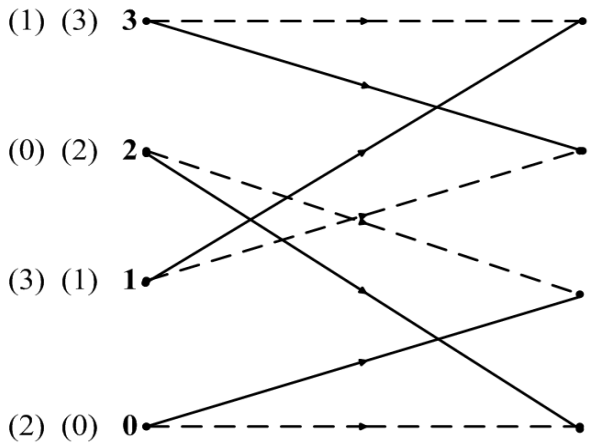

Figure 3-1: Trellis diagram of the 1/2-rate 4-state systematic encoder for $d = 1$ [23, Fig. 18].

The top-to-bottom arrangement of the trellis paths emerging from each state corresponds to the left-to-right arrangement of trellis path labels at that state. Note that trellis path labels are enclosed in brackets, while trellis states are written in bold font in both Figure 3-1 and Figure 3-2. Trellis

path labels have a decimal to binary correspondence with the binary (d+1)-tuple outputs of the systematic trellis encoder, for example in Figure 3-1, (0) corresponds to 00, (1) corresponds to 01, (2) corresponds to 10, etc., while in Figure 3-2, (0) corresponds to 000, (1) corresponds to 001, etc. Each trellis path label (k), where $k \in [0: 2^{d+1} - 1]$, further corresponds to the high-rate STBC formulated in (3.3) as $\boldsymbol{B}_k$.

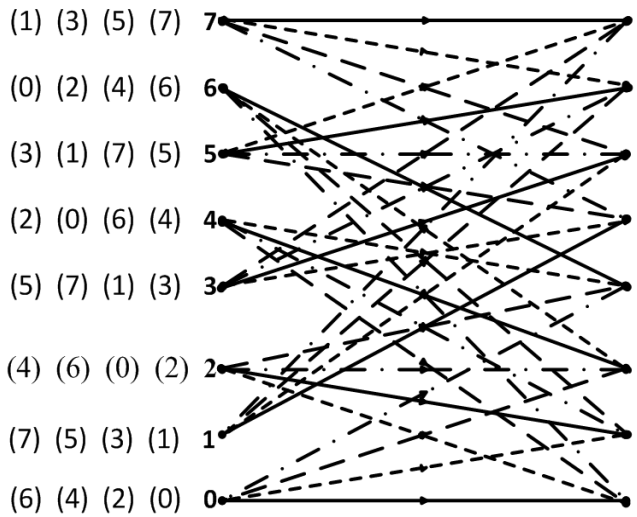

Figure 3-2: Trellis diagram of the 2/3-rate 8-state systematic encoder for $d = 2$ [23, Fig. 4].

As a bit mapping example, consider the $2/3$-rate systematic trellis encoder illustrated in Figure 3-3, at state 0.

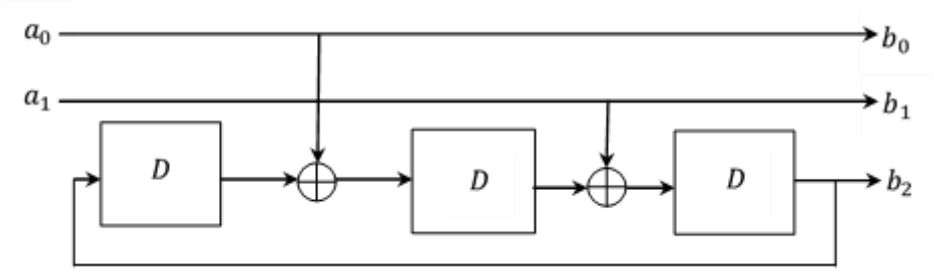

Figure 3-3: 2/3-rate 8-state systematic encoder for $d = 2$ [23, Fig. 3].

Applying the input $a_0a_1 = 00$, which corresponds to solid lines in Figure 3-2, yields an output $b_0b_1b_2 = 000$. According to the decimal to binary correspondence stated previously, the output 000 corresponds to the trellis path label (0), therefore $\boldsymbol{B}_0$ is selected for further encoding. In the same manner, applying the inputs 01, 10 or 11 respectively, denoted by short-dashed lines, long-dashed lines and dashed with dots lines at state 0 selects $\boldsymbol{B}_2$, $\boldsymbol{B}_4$ or $\boldsymbol{B}_6$, respectively. Similarly, applying the input 0 denoted by dashed lines in Figure 3-1, to the $1/2$-rate systematic trellis encoder at state 0 yields the output 00, which further selects $\boldsymbol{B}_0$. Applying the input bit 1 instead, denoted by solid lines, yields the output 10 which further selects $\boldsymbol{B}_2$. This encoding example portrays that the high-rate STBC selected in each trellis encoding segment is a function

of the state of the encoder and the bit stream that is applied to the input of the trellis encoder at that particular instant. Therefore, the high-rate space-time codeword transmitted at any t^{th} instant is encoded according to the selected high-rate STBC of (3.3) as follows:

$$\boldsymbol{X}_{k,t} = \begin{bmatrix} x_1 & x_2 e^{j\theta_k} \\ -x_2^* & x_1^* e^{j\theta_k} \end{bmatrix} \quad 0 \le k \le 2^{d+1} - 1 \tag{3.5}$$

where the rotational angle θ_k is a function of the trellis state and additional bits at that instant.

3.2 System Model

Consider an $N_T \times N_R$ TC-DSTBC system with $N_T = 2, N_R \geq N_T$, as depicted in Figure 3-4.

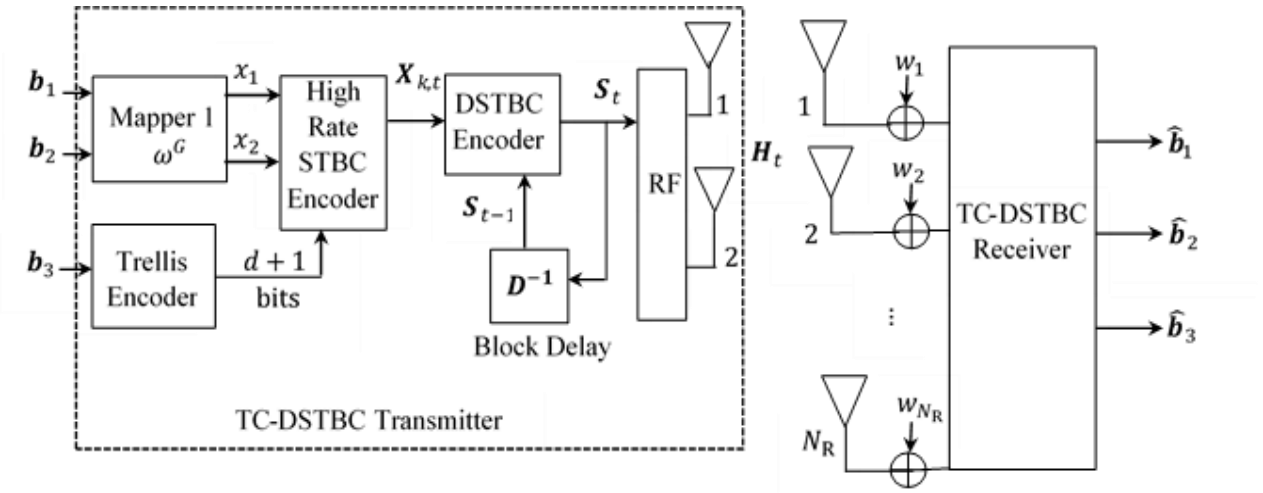

Figure 3-4: System model for TC-DSTBC

Message bits are partitioned into groups of $2m + d$ bits, where $m = \log_2 M$. In this dissertation, only $d = 1$ and $d = 2$ are considered. At the t^{th} time instant, the first $2m$ bits are further partitioned into two bit streams, $\boldsymbol{b}_1 = [b_{1,1}\ b_{1,2}\ \cdots\ b_{1,m}]$ and $\boldsymbol{b}_2 = [b_{2,1}\ b_{2,2}\ \cdots\ b_{2,m}]$, each of length m. The two bit streams are fed into Mapper 1 (ω^G). Mapper 1 employs the Gray-coded labeling map depicted in Appendix B to respectively, map $\boldsymbol{b}_1$ and $\boldsymbol{b}_2$ onto M-QAM modulated symbols x_1 and x_2. We assume, as in Section 2.1.1, that each symbol is normalised such that $\mathrm{E}\{|x_1|^2\} = \mathrm{E}\{|x_2|^2\} = 1$. Thereafter, symbols x_1 and x_2 are fed into the high-rate STBC encoder. The additional bit stream $\boldsymbol{b}_3 = [b_{3,1}\ \cdots\ b_{3,d}]$, of length d, is fed into the $d/d+1$-rate 2^{d+1}-state systematic trellis encoder of [23] to produce $d + 1$ bits that select one of the 2^{d+1} high-rate STBCs of (3.3) according to the appropriate trellis diagram. Finally, the two symbols, x_1 and x_2, are encoded according to the selected high-rate STBC $\boldsymbol{B}_k$, yielding the codeword $\boldsymbol{X}_{k,t}$ of (3.5). In this dissertation, we employ tail bits to ensure that the encoding process over N successive encoding segments starts and ends at the first trellis state, where N is the trellis encoder depth.

Prior to transmission, $\boldsymbol{X}_{k,t}$ undergoes a differential encoding process formulated from [3] as follows:

$$\boldsymbol{S}_t = \left(\beta_{t-1}\right)^{-1} \boldsymbol{X}_{k,t} \boldsymbol{S}_{t-1},\ t \in [1{:}N] \tag{3.6}$$

where $\boldsymbol{S}_{t-1}$ is the DSTBC transmitted at the time instant prior to t. The power normalisation factor $(\beta_{t-1})^{-1}$, is defined by $\beta_{t-1} = \sqrt{\|\boldsymbol{S}_{t-1}\|_F^2}$. The transmission process of N information bearing differential space-time codewords is initialised by sending the arbitrary STBC $\boldsymbol{S}_0$. The STBC $\boldsymbol{S}_0$ is set as $\boldsymbol{X}_{0,0}$, which is selected in random from the codebook $\boldsymbol{\chi}_0$ defined in Section 3.1.1.

The $2 \times N_{\mathrm{R}}$ received signal matrix $\boldsymbol{Y}_t$ is modelled as:

$$\boldsymbol{Y}_t = \sqrt{\rho/2}\, \boldsymbol{S}_t \boldsymbol{H}_t + \boldsymbol{W}_t,\ t \in [0{:}N] \tag{3.7}$$

where $\rho/2$ is the average SNR at each receive antenna, $\boldsymbol{H}_t$ is the $2 \times N_{\mathrm{R}}$ channel matrix and $\boldsymbol{W}_t$ is the $2 \times N_{\mathrm{R}}$ received AWGN matrix. The complex entries of both $\boldsymbol{H}_t$ and $\boldsymbol{W}_t$ are i.i.d. Gaussian RVs distributed as $CN\ (0{,}1)$. The channels between the transmitter and the receiver are assumed to be Rayleigh quasi-static frequency-flat fading over $N+1$ DSTBCs, i.e. $\boldsymbol{H}_0 = \boldsymbol{H}_t,\ t \in [1{:}N]$. Therefore, (3.7) may be further expressed as:

$$\begin{aligned} \boldsymbol{Y}_t &= \sqrt{\rho/2}\,(\beta_{t-1})^{-1} \boldsymbol{X}_{k,t} \boldsymbol{S}_{t-1} \boldsymbol{H}_t + \boldsymbol{W}_t \\ &= (\beta_{t-1})^{-1} \boldsymbol{X}_{k,t} (\boldsymbol{Y}_{t-1} - \boldsymbol{W}_{t-1}) + \boldsymbol{W}_t \\ &= (\beta_{t-1})^{-1} \boldsymbol{X}_{k,t} \boldsymbol{Y}_{t-1} + \widetilde{\boldsymbol{W}}_t \end{aligned} \tag{3.8}$$

where $\widetilde{\boldsymbol{W}}_t = \boldsymbol{W}_t - (\beta_{t-1})^{-1} \boldsymbol{X}_{k,t} \boldsymbol{W}_{t-1}$.

The VA-based decoding technique at the receiver of the TC-DSTBC system determines the most likely transmitted sequence of $\widehat{\boldsymbol{X}}_{k,t}$ by employing the ML estimation method to minimise the branch metric $bm_t^{i,l}$ in (3.9) for each possible state i to state l transition at the t^{th} decoding stage.

$$bm_t^{i,l} = \operatorname{argmin}_{\widehat{\boldsymbol{X}}_{k,t} \in \boldsymbol{\chi}_k} \left\| \boldsymbol{Y}_t - \left(\beta_{t-1}\right)^{-1} \widehat{\boldsymbol{X}}_{k,t} \boldsymbol{Y}_{t-1} \right\|_F^2, t \in [1{:}N] \tag{3.9}$$

where $i, l \in [0{:}\,2^{d+1}-1]$, the codebook $\boldsymbol{\chi}_k$ contains all high-rate space-time codewords of type $\boldsymbol{B}_k$ corresponding to the state i to state l trellis path of the appropriate trellis diagram. At each state l, the path metric pm_t^l given by (3.10) is minimised to determine the survivor path, where i denotes all the possible previous states with respect to state l.

$$pm_t^l = \operatorname{argmin}_i (pm_{t-1}^i + bm_t^{i,l}) \quad i, l \in \left[0{:}\,2^{d+1}-1\right], t \in [1{:}N] \tag{3.10}$$

For example, consider the four trellis state transitions in Figure 3-2 that merge at the trellis state 0 during the third decoding segment. Let path 1 with metric pm_2^0, path 2 with metric pm_2^2, path 3 with metric pm_2^4 and path 4 with metric pm_2^6 be the state 0 to state 0 path, state 2 to state 0 path, state 4 to state 0 path and state 6 to state 0 path, respectively. Path 1, path 2, path 3 and path 4 correspond to branch metrics $bm_3^{0,0}$, $bm_3^{2,0}$, $bm_3^{4,0}$ and $bm_3^{6,0}$, respectively. The VA decoder minimises $bm_3^{0,0}$ according to (3.9) by performing an exhaustive search over all codewords of $\boldsymbol{\chi}_0$. Similarly, exhaustive searches over all codewords of the codebooks $\boldsymbol{\chi}_2$, $\boldsymbol{\chi}_4$ and $\boldsymbol{\chi}_6$ are performed to minimise $bm_3^{2,0}$, $bm_3^{4,0}$ and $bm_3^{6,0}$, respectively. To find the survivor path, the updated path metrics $pm_2^0 + bm_3^{0,0}$, $pm_2^2 + bm_3^{2,0}$, $pm_2^4 + bm_3^{4,0}$ and $pm_2^6 + bm_3^{6,0}$ are compared. If $pm_2^0 + bm_3^{0,0}$ is less than all the other updated path metrics, the new path metric is updated as $pm_3^0 = pm_2^0 + bm_3^{0,0}$. Thereafter, the decoder stores the codeword that minimised $bm_3^{0,0}$ together with path 1 as the survivor path, while the other paths are discarded.

Alternately, if $pm_2^6 + bm_3^{6,0}$ is the lowest, the new path metric is updated as $pm_3^0 = pm_2^6 + bm_3^{6,0}$. Thereafter, the decoder stores the codeword that minimised $bm_3^{6,0}$ together with path 4 as the survivor path, while the other paths are discarded.. Similar processes are performed at the other trellis states and decoding segments. The use of tail bits ensures that only one survivor trellis path or sequence of decoded high-rate space-time codewords remains after N decoding segments.

3.3 Simulation and Analytical Results

In this section, the simulation results for $2 \times N_R$ TC-DSTBC, $2 \times N_R$ CDD-DSTBC [3] and $2 \times N_R$ coherent Alamouti STBC together with analytical results for $2 \times N_R$ coherent Alamouti STBC over i.i.d. Rayleigh frequency-flat quasi-static fading channels are presented and compared for the following modulation schemes and additional bit numbers (d):

1. 16-QAM with $d = 1$

2. 64-QAM with $d = 1$

3. 16-QAM with $d = 2$

4. 64-QAM with $d = 2$

The aim of this section is to:

a. Demonstrate that the more bandwidth efficient TC-DSTBC system retains the BER performance of the CDD-DSTBC system.

b. Demonstrate that the TC-DSTBC also suffers a SNR penalty when compared to the coherent Alamouti STBC system.

The average BER performance of the coherent Alamouti STBC system was obtained by evaluating the closed form expression in (2.7). The simulation results for the coherent Alamouti STBC are given by the model presented in [2]. Monte Carlo simulations were performed for both TC-DSTBC and CDD-DSTBC. All BER performance comparisons are made at a BER value of 10^{-5}. For simulation purposes, the fading channel and noise parameters were defined in line with those presented in (3.7) in Section 3.2. We also assumed that $N_{\mathrm{R}} = 4$; $N = 100$; the CSI is not known at the receiver; there is sufficient separation of transmit antennas such that all channel gains are independent of each other; MRC reception is employed.

The results for the 16QAM TC-USTLD system with $d = 1$ and $d = 2$ are presented in Figure 3-5 and Figure 3-7, respectively, while the results for the 64QAM TC-USTLD system with $d = 1$ and $d = 2$ are presented in Figure 3-6 and Figure 3-8, respectively.

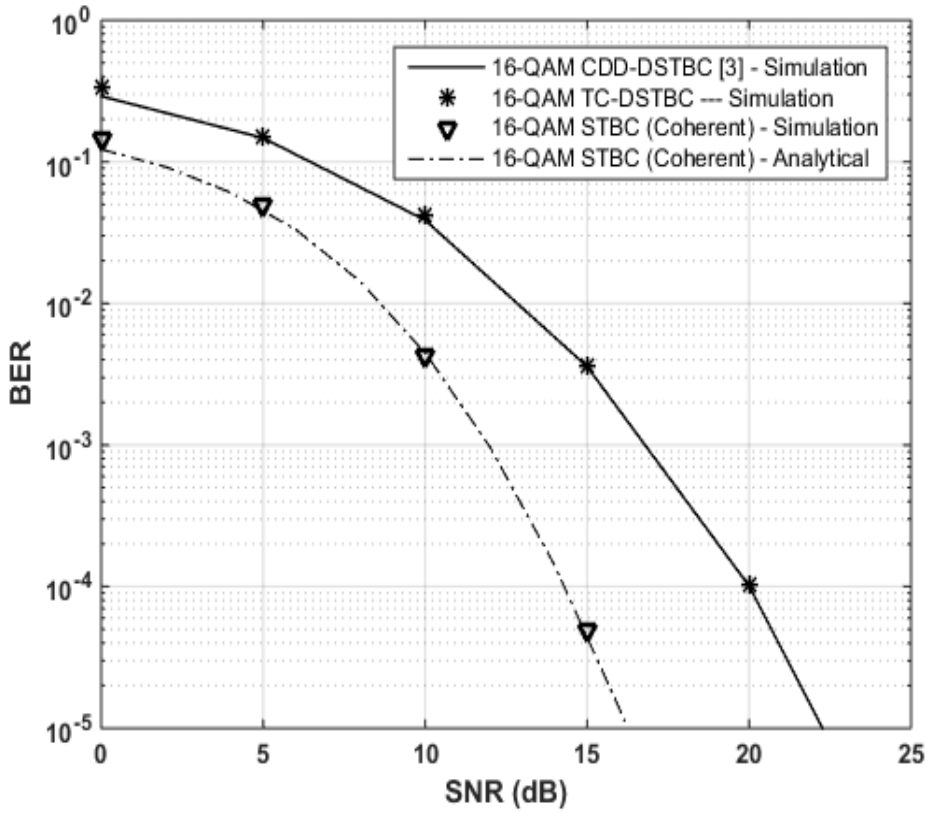

Figure 3-5: BER performance of the TC-DSTBC, CDD-DSTBC and coherent Alamouti STBC systems for 16-QAM, d = 1 with analytical results of the coherent Alamouti STBC system.

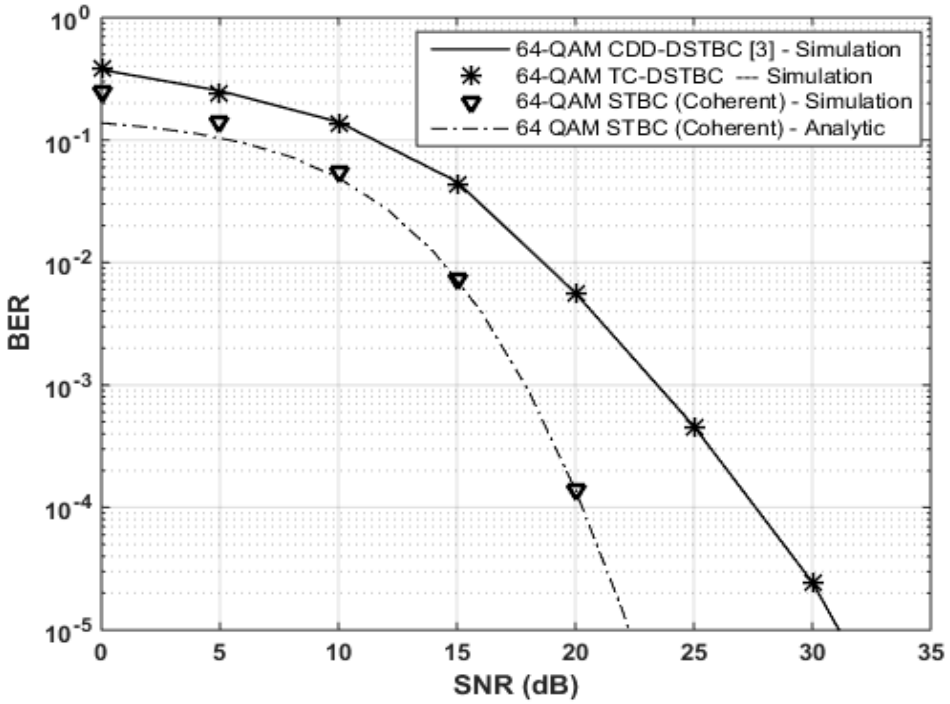

Figure 3-6: BER performance of the TC-DSTBC, CDD-DSTBC and coherent Alamouti STBC systems for 64-QAM, d = 1 with analytical results of the coherent Alamouti STBC system

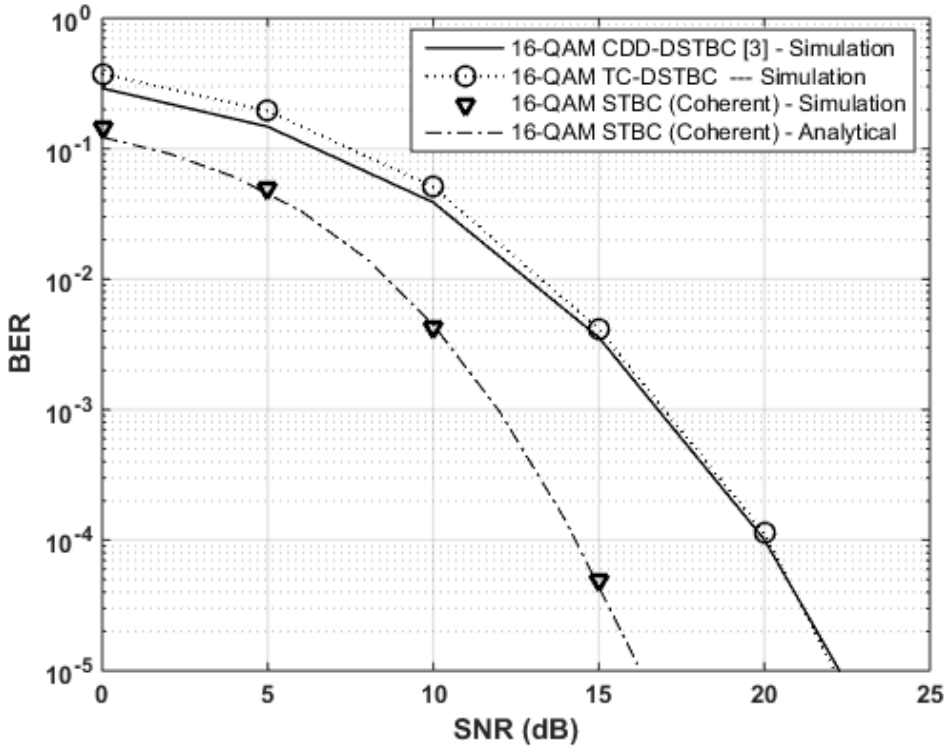

Figure 3-7: BER performance of the TC-DSTBC, CDD-DSTBC and coherent Alamouti STBC systems for 16-QAM, d = 2 with analytical results of the coherent Alamouti STBC system

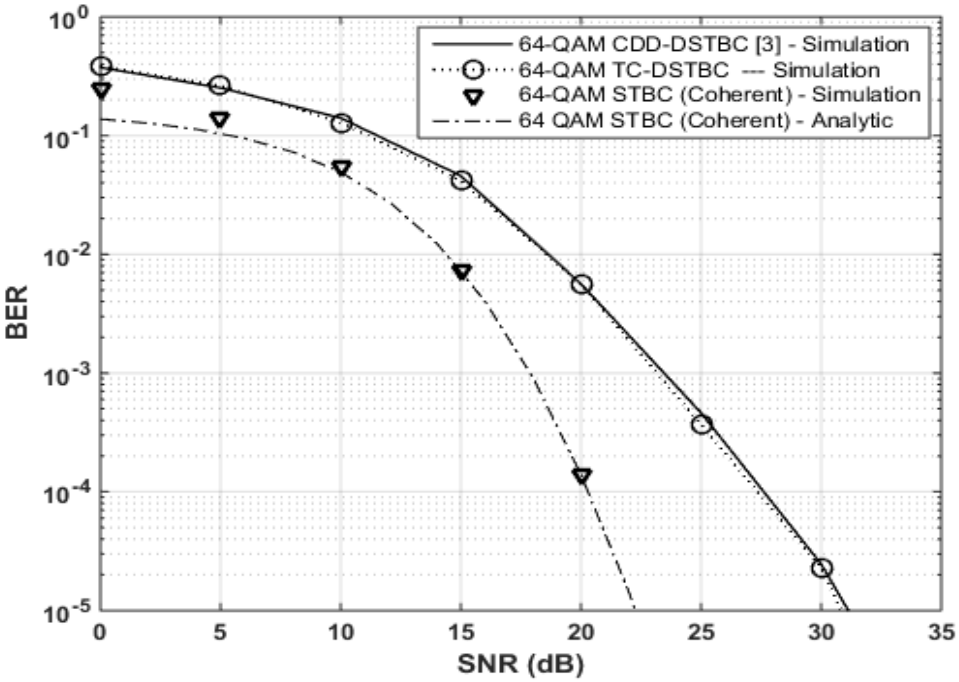

Figure 3-8: BER performance of the TC-DSTBC, CDD-DSTBC and coherent Alamouti STBC systems for 64-QAM, d = 2 with analytical results of the coherent Alamouti STBC system

It can be observed that, at high SNR values, the BER performance of TC-DSTBC converges to that of CDD-DSTBC down to the average BER of 10^{-5}. The scheme with 64QAM tightly matches the error performance of the corresponding CDD-DSTBC at all SNR values.

It is also evident that there is a performance gap of approximately 5dB between the coherent Alamouti STBC and the DSTBCs with 16QAM in Figure 3-5 and Figure 3-7, which is similar to the SNR gap shown in [3, Fig. 1(a)]. As with an SNR gap shown in [3, Fig. 1(a)], the SNR gap increases further with an increase in the order of M-QAM. In simulation results presented in Figure 3-6 and Figure 3-8, the SNR gap between the coherent STBC and DSTBCs with 64QAM exceeds 5dB in the high SNR region. However, TC-DSTBC achieves better bandwidth efficiency compared to CDD-DSTBC, as shown in Table 3-2.

The comparison of bandwidth efficiency between TC-DSTBC and the conventional DSTBC show that TC-DSTBC achieves a minimum of 12.5% and 8.3% increase in bandwidth efficiency for 16-QAM and 64-QAM, respectively.

Table 3-2: Bandwidth efficiency comparison of TC-DSTBC and CDD-DSTBC.

Scheme	**Bandwidth Efficiency (b/s/Hz)**	**Percentage (%) Increase**
16-QAM CDD-DSTBC [2]	4	-
16-QAM TC-DSTBC with d=1	4.5	12.5
16-QAM TC-DSTBC with d=2	5	25
64-QAM CDD-DSTBC [2]	6	-
64-QAM TC-DSTBC with d=1	6.5	8.3
64-QAM TC-DSTBC with d=2	7	16.7

3.4 Chapter Summary and Conclusion

In this chapter, we developed a technique for enhancing the bandwidth efficiency for STBC wireless communication systems. The technique was applied to a differential Alamouti scheme resulting in a high-rate DSTBC system with two transmit antennas in the form of TC-DSTBC. TC-DSTBC retains the BER performance of a conventional DSTBC system dubbed CDD-DSTBC under the same fading channel and AWGN conditions, while achieving a higher bandwidth efficiency. However, there is a trade-off. Bandwidth efficiency is enhanced at the expense of an increase of the computational complexity at the receiver. The increase of the computational complexity is due to use of a high-complexity (HC) VA-based decoder at the receiver.

As demonstrated in this chapter, TC-DSTBC has a superior bandwidth efficiency i.e. it achieves high data rates without compromising the bandwidth, hence TC-DSTBC and the technique for enhancing the bandwidth efficiency for space-time block coded wireless communication systems can be considered as the most suitable solutions for improving data rates without compromising the link reliability. In the next chapter, the application of the bandwidth efficiency improvement technique to USTLD is presented.

4. Enhanced Uncoded Space-time Labeling Diversity

Motivated by the bandwidth efficiency advantage of the TC-DSTBC system over the conventional Alamouti DSTBC system, this chapter extends the trellis code-aided bandwidth efficiency improvement technique to the recently developed USTLD system in the form of enhanced USTLD (E-USTLD). It is expected that the E-USTLD will retain the BER performance of the conventional USTLD system under the same fading channel and AWGN conditions. This chapter presents the mathematical model and derives a closed form lower bound expression to predict the average BER for the M-QAM E-USTLD system over i.i.d. Rayleigh frequency-flat fading channels.

4.1 System Model

Consider an $N_{\mathrm{T}} \times N_{\mathrm{R}}$ M-QAM E-USTLD system with d additional bits, $N_{\mathrm{T}} = 2, N_{\mathrm{R}} \geq N_{\mathrm{T}}$, as illustrated in Figure 4-1.

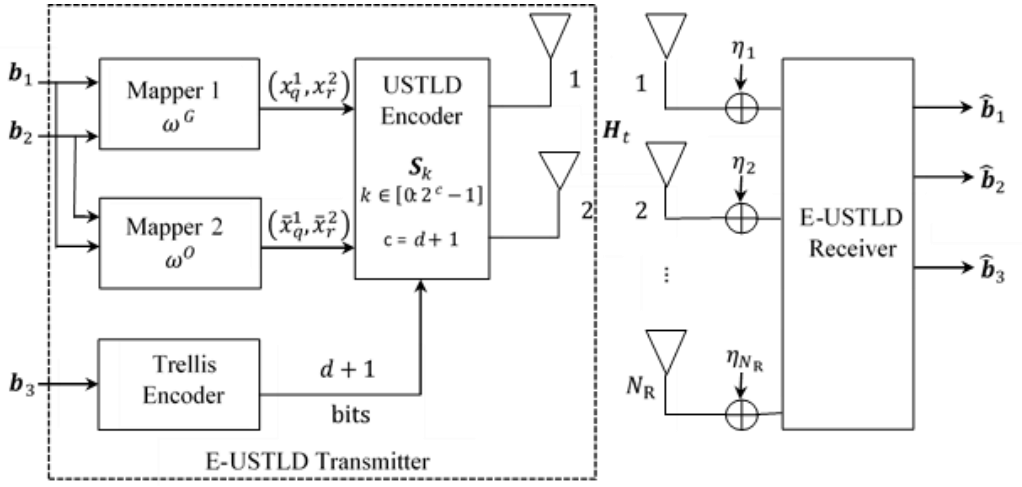

Figure 4-1: System model for E-USTLD

In this dissertation, we consider $d = 1$ and $d = 2$ only. Information bits are divided into blocks of $2m + d$ bits, where $m = \log_2 M$. Each block is further partitioned into three substreams, $\boldsymbol{b}_1 = [b_1\ b_2\ \cdots\ b_m]$, $\boldsymbol{b}_2 = [b_{m+1}\ b_{m+2}\ \cdots\ b_{2m}]$ and $\boldsymbol{b}_3 = [b_{2m+1}\ \cdots\ b_{2m+d}]$. The bit streams $\boldsymbol{b}_1$ and $\boldsymbol{b}_2$ are fed into two mappers, Mapper 1 that employs the Gray-coded labeling map ω^G and Mapper 2 that employs the optimized labeling map ω^O as in Xu et al [17], with each mapper mapping input bits onto two M-QAM symbols, yielding symbol pairs (x_q^1, x_r^2) and $(\bar{x}_q^1, \bar{x}_r^2)$, respectively, where $q = 1 + \sum_{k=1}^{m} b_k 2^{m-k}$ and $r = 1 + \sum_{k=m+1}^{2m} b_k 2^{m-k}$. Note, the labeling maps used in this dissertation are given in Appendix B. We assume $\mathrm{E}\left\{\left|x_q^1\right|^2\right\} = \mathrm{E}\{|x_r^2|^2\} = \mathrm{E}\left\{\left|\bar{x}_q^1\right|^2\right\} = \mathrm{E}\{|\bar{x}_r^2|^2\} = 1$. Symbol pairs from the two mappers are fed into the USTLD encoder, simultaneously with $d + 1$ output bits of the trellis encoder. The output bits of the trellis encoder

are a function of the third bit stream $\boldsymbol{b}_3$. These output bits select one of the 2^{d+1} available high-rate USTLD codes as discussed in the next section. Finally, symbol pairs are encoded according to the selected high-rate code prior to transmission. The transmitted high-rate codeword is defined as $\boldsymbol{S}_k = [\boldsymbol{s}_1^k \quad \boldsymbol{s}_2^k]$, $0 \leq \mathrm{k} \leq 2^{d+1} - 1$ where $\boldsymbol{s}_1^k$ and $\boldsymbol{s}_2^k$ are column vectors of symbols that are transmitted in time slot 1 and 2, respectively. The column vectors are defined in the next section. Tail bits are employed to ensure that the trellis encoding process for N successive encoding segments starts and ends at the first trellis state.

The channel is assumed to be Rayleigh frequency-flat fading, and is known at the receiver. The channel takes on independent values in the two time slots ($\boldsymbol{H}_1 = \boldsymbol{H}_2$) [17]. The $N_\mathrm{R} \times 1$ received signal vectors are modelled as:

$$\boldsymbol{y}_1 = \sqrt{\frac{\rho}{2}}\boldsymbol{H}_1\boldsymbol{s}_1^k + \boldsymbol{\eta}_1 \tag{4.1}$$

$$\boldsymbol{y}_2 = \sqrt{\frac{\rho}{2}}\boldsymbol{H}_2\boldsymbol{s}_2^k + \boldsymbol{\eta}_2 \tag{4.2}$$

where $\rho/2$ is the average SNR at each receive antenna, $\boldsymbol{H}_t$ is the $N_\mathrm{R} \times 2$ channel matrix, $\boldsymbol{\eta}_t$ is the $N_\mathrm{R} \times 1$ received AWGN vector. The entries of $\boldsymbol{H}_t$ and $\boldsymbol{\eta}_t$ are i.i.d. RVs distributed as $CN(0,1)$. $\boldsymbol{H}_t$ is also defined as $\boldsymbol{H}_t = [h_t^1 \quad h_t^2]$, $t \in [1\colon 2]$, where, $h_t^i = [h_t^{1,i}\ h_t^{2,i} \cdots h_t^{N_\mathrm{R},i}]^T$, $i \in [1\colon 2], t \in [1\colon 2]$.

At the receiver, the VA-based coherent detector is employed to determine the likely transmitted codeword sequence. At the n^{th} decoding segment, the detector minimises the ML branch metric in (4.3) to determine the high-rate codeword that corresponds to each possible state i to state l transition.

$$bm_n^{i,l} = \mathrm{argmin}_{(\hat{\boldsymbol{s}}_1^k \quad \hat{\boldsymbol{s}}_2^k) \in \boldsymbol{\varsigma}_k} \left(\left\| \boldsymbol{y}_1 - \sqrt{\frac{\rho}{2}}\boldsymbol{H}_1\hat{\boldsymbol{s}}_1^k \right\|_F^2 + \left\| \boldsymbol{y}_2 - \sqrt{\frac{\rho}{2}}\boldsymbol{H}_2\hat{\boldsymbol{s}}_2^k \right\|_F^2 \right), n \in [1\colon N] \tag{4.3}$$

where $i, l \in [0\colon 2^{d+1} - 1]$ and $\boldsymbol{\varsigma}_k, k \in [0\colon 2^{d+1} - 1]$, is the codebook of all ordered high-rate codewords of type $\boldsymbol{S}_k$ corresponding to the state i to state l trellis path. The detector then updates the survivor path metric at each state by minimising the metric defined as:

$$pm_n^l = \mathrm{argmin}_i\left(pm_{n-1}^i + bm_n^{i,l}\right) \quad i, l \in [0\colon 2^{d+1} - 1], n \in [1\colon N] \tag{4.4}$$

As an example, consider the trellis paths in Figure 3-1 that remerge in the trellis state 0 at the third decoding segment. Let path 1 with metric pm_2^0 be the state 0 to state 0 path and path 2 with metric pm_2^2 be the state 2 to state 0 path. Path 1 and path 2 correspond to branch metrics $bm_3^{0,0}$ and $bm_3^{2,0}$, respectively. The detector minimises $bm_3^{0,0}$ according to (4.3) by performing an exhaustive search

over all codewords of the codebook $\boldsymbol{\varsigma}_0$. Similarly, an exhaustive search over all codewords of the codebook $\boldsymbol{\varsigma}_2$ is performed to minimise $bm_3^{2,0}$. To find the survivor path, the updated path 1 metric given by $pm_2^0 + bm_3^{0,0}$ is compared with the updated path 2 metric given by $pm_2^2 + bm_3^{2,0}$. If $pm_2^0 + bm_3^{0,0} < pm_2^2 + bm_3^{2,0}$, the new path metric is updated as $pm_3^0 = pm_2^0 + bm_3^{0,0}$. Path 1 is then stored as the survivor path together with the codeword that minimised $bm_3^{0,0}$, while path 2 is discarded. Alternately, if $pm_2^0 + bm_3^{0,0} > pm_2^2 + bm_3^{2,0}$, the new path metric is updated as $pm_3^0 = pm_2^2 + bm_3^{2,0}$. Path 2 is then stored as the survivor path together with the codeword that minimised $bm_3^{2,0}$, while path 1 is discarded. Similar processes are performed at the other trellis states and decoding segments.

4.2 High-rate USTLD Code Construction and Mapping

In this section, we introduce a high-rate USTLD code that retains the error performance of the existing USTLD. The high-rate USTLD code construction is similar to that of the TC-DSTBC that has been discussed in Section 3.1.1. The USTLD code $\boldsymbol{X}$ proposed by Xu et al [17] is expanded by multiplying it by unitary matrices. In order to send d additional bits per USTLD codeword, a total of 2^{d+1} unitary matrices is required. This number of unitary matrices ensures that the cardinality of high-rate USTLD codes satisfies the redundancy requirement for trellis coding [23]. We employ unitary matrices with the structure shown in (3.2), where the rotational angle is defined as $\theta_k = \frac{2\pi k}{2^{d+1}}$, for all $k \in [0: 2^{d+1} - 1]$. The resulting high-rate USTLD codes are defined as:

$$\boldsymbol{S}_k = \boldsymbol{U}_k \boldsymbol{X} \tag{4.5}$$

where $\boldsymbol{X} = [\boldsymbol{x}_1\ \boldsymbol{x}_2]$, $\boldsymbol{x}_1 = \left[x_q^1\ \ x_r^2\right]^T$, $\boldsymbol{x}_2 = \left[\bar{x}_r^2\ \ \bar{x}_q^1\right]^T$ [17]. The high-rate code is also expressed as $\boldsymbol{S}_k = \left[\boldsymbol{s}_1^k\ \ \boldsymbol{s}_2^k\right]$, where the column vectors are defined as $\boldsymbol{s}_1^k = \left[x_q^1\ \ x_r^2\ \right]^T$ and $\boldsymbol{s}_2^k = \left[\bar{x}_r^2 \mathrm{e}^{\mathrm{j}\theta_k}\ \ \bar{x}_q^1 \mathrm{e}^{\mathrm{j}\theta_k}\right]^T$. The rotational angle θ_k encodes additional bits. We assume that M^2 distinct codewords of each high-rate USTLD code $\boldsymbol{S}_k$, $k \in [0: 2^{d+1} - 1]$, are contained in the codebook denoted by $\boldsymbol{\varsigma}_k$. For example, the codebook $\boldsymbol{\varsigma}_0$ contains M^2 distinct codewords of type $\boldsymbol{S}_0$, which have the same rotational angle $\theta_0 = 0$. Similarly, $\boldsymbol{\varsigma}_1$ contains codewords of type $\boldsymbol{S}_1$, which have the same rotational angle $\theta_1 = \frac{2\pi}{2^{d+1}}$, etc.

In order to avoid the degradation of the error performance of the expanded USTLD code, trellis code-aided mapping of additional bits to USTLD codes is employed. The trellis coding in E-USTLD effectively maximizes the sum of product distances between possible sequences of transmitted high-rate codewords. Note that the product distance is the main performance parameter of USTLD at high SNR and large N_{R} [17]. We employ the same $d/d+1$-rate 2^{d+1}-

state systematic trellis encoders as in Section 3.1.3 to map d additional bits to high-rate USTLD codes, hence, the mapping of additional bits for $d = 1$ and $d = 2$ is done according to the trellis diagrams of Figure 3-1 and Figure 3-2, respectively.

The trellis encoders employed ensure that each trellis state transition is associated with only one high-rate code. Trellis path labels correspond to the binary $(d + 1)$-tuple outputs of systematic trellis encoders, which further correspond to high-rate codes as shown in Table 4-1.

Table 4-1: Relationship between trellis path labels, systematic trellis encoder outputs and high-rate codes.

Trellis path label	**$1/2$-rate trellis encoder output**	**$2/3$-rate trellis encoder output**	**High-rate USTLD code**
(0)	00	000	$\boldsymbol{S}_0$
(1)	01	001	$\boldsymbol{S}_1$
(2)	10	010	$\boldsymbol{S}_2$
(3)	11	011	$\boldsymbol{S}_3$
(4)		100	$\boldsymbol{S}_4$
(5)		101	$\boldsymbol{S}_5$
(6)		110	$\boldsymbol{S}_6$
(7)		111	$\boldsymbol{S}_7$

We use an example to demonstrate the trellis code-aided mapping of additional bits to high-rate USTLD codes. Consider the $1/2$-rate systematic trellis encoder illustrated in Figure 4-2, at state 0.

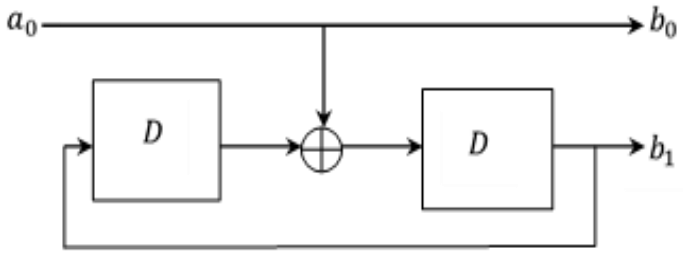

Figure 4-2: 1/2-rate 4-state systematic encoder for $d = 1$ [23, Fig. 17].

Applying an input $a_0 = 0$, which corresponds to dashed lines in Figure 3-1, yields an output $b_0 b_1 = 00$. According to Table 4-1, the output 00 selects $\boldsymbol{S}_0$ for transmission. Applying input $a_0 = 1$ instead, denoted by solid lines, yields the output 10 which further selects $\boldsymbol{S}_2$. Similarly, applying the input 00 denoted by solid lines in Figure 3-2, to the $2/3$-rate systematic trellis encoder at state 0 yields the output 000, which further selects $\boldsymbol{S}_0$. Applying the input 01

denoted by short-dashed lines, 10 denoted by long-dashed lines or 11 denoted by dashed with dots lines at state 0 selects $\boldsymbol{S}_2$, $\boldsymbol{S}_4$ or $\boldsymbol{S}_6$, respectively. This example demonstrates that the high-rate USTLD code selected in each trellis encoding segment is a function of the bit stream that is applied to the input of the trellis encoder and the state of the encoder at that instant.

4.3 Error Performance Analysis of M-QAM E-USTLD

In this section, we derive the theoretical bit error performance for M-QAM E-USTLD in i.i.d. Rayleigh frequency-flat fading conditions. The employed detector estimates the encoding trellis path and transmitted symbol pairs. Consequently, the error performance of M-QAM E-USTLD depends on the error performances of the encoding trellis path and transmitted symbol pairs estimation processes. In order to simplify the subsequent analysis, we assume two independent estimation processes as in Naidoo et al [28]. Let P_b denote the bit error probability (BEP) of symbol pair estimation given that the encoding trellis path is estimated correctly and P_t the BEP of encoding trellis path estimation given that the symbol pair is estimated correctly. The overall average BEP is bounded by

$$P_e \geq P_b + P_t + P_b P_t \tag{4.6}$$

Naidoo et al [28] noted that the assumption of independent estimation processes represents an ideal scenario, therefore (4.6) corresponds to the best performance achievable (lower bound) by the M-QAM E-USTLD system.

4.3.1 Analytical BEP of Symbol Pair Estimation

As discussed previously it is assumed that the encoding trellis path is estimated correctly for symbol pair estimation. This assumption corresponds to the correct estimation of θ_k. As Xu et al suggested, at high SNR only one transmitted symbol pair is assumed to be detected with errors and the other transmitted symbol pair is correctly detected in the USTLD system [17]. In this section we assume that x_q^1 and $\bar{x}_q^1$ are detected with errors, while x_r^2 and $\bar{x}_r^2$ are detected correctly. The average BEP for symbol pair estimation is union bounded by

$$P_b \leq \frac{1}{N_a M(m+0.5d)} \sum_{q=1}^{M} \sum_{k=0}^{N_a-1} \sum_{\hat{q}\neq q}^{M} N_{\hat{q},q} P\left(\mathbf{S}_k \rightarrow \hat{\mathbf{S}}_k\right) \tag{4.7}$$

where N_a is the cardinality of rotational angles, $P\left(\mathbf{S}_k \rightarrow \hat{\mathbf{S}}_k\right)$ is the pairwise error probability (PEP) of choosing the codeword $\hat{\mathbf{S}}_k$ given that $\mathbf{S}_k$ was transmitted, $\hat{\mathbf{S}}_k = [\hat{s}_1^k \; \hat{s}_2^k]$, $\hat{s}_1^k = \left[x_{\hat{q}}^1 \quad x_r^2 \mathrm{e}^{\mathrm{j}\theta_k}\right]^T$, $\hat{s}_2^k = [\bar{x}_r^2 \quad \bar{x}_{\hat{q}}^1 \mathrm{e}^{\mathrm{j}\theta_k}]^T$, $N_{\hat{q},q}$ is the number of bit errors between symbols x_q^1 and

$x_{\hat{q}}^1$, and $m + 0.5d$ is the average number of information bits conveyed by one symbol. The conditional PEP for the symbol pair has been formulated in [17] and is expressed as:

$$P(\mathbf{S}_k \to \hat{\mathbf{S}}_k) = \frac{1}{2n}\left[\frac{1}{2}\left(\frac{8}{\rho d_1 + 8}\right)^{N_R}\left(\frac{8}{\rho d_2 + 8}\right)^{N_R} + \sum_{i=1}^{n-1}\left(\frac{8S_i}{\rho d_1 + 8S_i}\right)^{N_R}\left(\frac{8S_i}{\rho d_2 + 8S_i}\right)^{N_R}\right] \tag{4.8}$$

where $S_i = 2\sin^2\frac{i\pi}{2n}$, $d_1 = \left|x_{\hat{q}}^1 - x_q^1\right|^2$, $d_2 = \left|\bar{x}_{\hat{q}}^1 - \bar{x}_q^1\right|^2$ and n is the number of iterations for convergence ($n > 10$) [29].

4.3.2 Analytical BEP of Encoding Trellis Path (additional bit) Estimation

As discussed before it is assumed that both symbols x_q^1 and x_r^2 are detected correctly for encoding trellis path estimation. To derive the average BEP of trellis path estimation, we introduce the subscript i to the expanded received signals expressions in (4.1) and (4.2) to distinguish between the received signals resulting from different successive encoding segments. Resulting expressions are shown in (4.9) and (4.10).

$$\boldsymbol{y}_{1,i} = \sqrt{\frac{\rho}{2}}\,\boldsymbol{h}_{1,i}^1 x_{q_i}^1 + \sqrt{\frac{\rho}{2}}\,\boldsymbol{h}_{1,i}^2 x_{r_i}^2 \mathrm{e}^{\mathrm{j}\theta_{k_i}} + \boldsymbol{\eta}_{1,i} \tag{4.9}$$

$$\boldsymbol{y}_{2,i} = \sqrt{\frac{\rho}{2}}\,\boldsymbol{h}_{2,i}^1 \bar{x}_{r_i}^2 + \sqrt{\frac{\rho}{2}}\,\boldsymbol{h}_{2,i}^2 \bar{x}_{q_i}^1 \mathrm{e}^{\mathrm{j}\theta_{k_i}} + \boldsymbol{\eta}_{2,i} \tag{4.10}$$

We assume that the shortest error event path dominates the error performance as in classical trellis coded modulation [22]. Therefore, for the high-rate scheme with one additional bit, the error performance is dominated by trellis paths that diverge in one state and remerge after a minimum of three state transitions. Similarly, trellis paths that remerge after a minimum of two state transitions dominate the error performance of the scheme with two additional bits. The average BEP for trellis path estimation for the scheme with one additional bit is union bounded by:

$$P_t \le \frac{1}{zM^6 d}\sum_{q_1=1}^{M}\sum_{r_1=1}^{M}\sum_{q_2=1}^{M}\sum_{r_2=1}^{M}\sum_{q_3=1}^{M}\sum_{r_3=1}^{M} N_f P(t_{k\to g} \to \hat{t}_{k\to g}) \tag{4.11}$$

while for a scheme with two additional bits, the ABEP for trellis path estimation is bounded by:

$$P_t \le \frac{1}{zM^4 d}\sum_{q_1=1}^{M}\sum_{r_1=1}^{M}\sum_{q_2=1}^{M}\sum_{r_2=1}^{M} N_f P(t_{k\to g} \to \hat{t}_{k\to g}) \tag{4.12}$$

where z is the minimum number of state transitions it takes for two trellis paths to remerge, $P(t_{k\to g} \to \hat{t}_{k\to g})$ is the PEP of choosing $\hat{t}_{k\to g}$ as the decoding trellis path given that $t_{k\to g}$ was the encoding trellis path, and $N_f = 2$ is the number of bit errors between the trellis paths $t_{k\to g}$ and $\hat{t}_{k\to g}$. The conditional PEP for the trellis path pair may be formulated as:

$$P(t_{k\to g} \to \hat{t}_{k\to g}|\boldsymbol{H}_1\boldsymbol{H}_2) = P\left(\sum_{i=1}^{z}\left\{\left\|\boldsymbol{y}_{1,i} - \sqrt{\frac{\rho}{2}}\,\boldsymbol{h}_{1,i}^{1}x_{q_i}^{1} - \sqrt{\frac{\rho}{2}}\,\boldsymbol{h}_{2,i}^{1}x_{r_i}^{2}\mathrm{e}^{\mathrm{j}\theta_{\hat{k}_i}}\right\|_F^2 + \left\|\boldsymbol{y}_{2,i} - \sqrt{\frac{\rho}{2}}\,\boldsymbol{h}_{2,i}^{1}\bar{x}_{r_i}^{2} - \sqrt{\frac{\rho}{2}}\,\boldsymbol{h}_{2,i}^{2}\bar{x}_{q_i}^{1}\mathrm{e}^{\mathrm{j}\theta_{\hat{k}_i}}\right\|_F^2\right\} < \sum_{i=1}^{z}\left\{\left\|\boldsymbol{y}_{1,i} - \sqrt{\frac{\rho}{2}}\,\boldsymbol{h}_{1,i}^{1}x_{q_i}^{1} - \sqrt{\frac{\rho}{2}}\,\boldsymbol{h}_{2,i}^{1}x_{r_i}^{2}\mathrm{e}^{\mathrm{j}\theta_{k_i}}\right\|_F^2 + \left\|\boldsymbol{y}_{2,i} - \sqrt{\frac{\rho}{2}}\,\boldsymbol{h}_{2,i}^{1}\bar{x}_{r_i}^{2} - \sqrt{\frac{\rho}{2}}\,\boldsymbol{h}_{2,i}^{2}\bar{x}_{q_i}^{1}\mathrm{e}^{\mathrm{j}\theta_{k_i}}\right\|_F^2\right\}\right) \tag{4.13}$$

Substituting (4-9) and (4-10) in (4-13) yields:

$$P(t_{k\to g} \to \hat{t}_{k\to g}|\boldsymbol{H}_1\boldsymbol{H}_2) = P\left(\sum_{i=1}^{z}\left\{\left\|\sqrt{\frac{\rho}{2}}\,\boldsymbol{h}_{2,i}^{1}x_{r_i}^{2}\left(\mathrm{e}^{\mathrm{j}\theta_{k_i}} - \mathrm{e}^{\mathrm{j}\theta_{\hat{k}_i}}\right) + \boldsymbol{\eta}_{1,i}\right\|_F^2 + \left\|\sqrt{\frac{\rho}{2}}\,\boldsymbol{h}_{2,i}^{2}\bar{x}_{q_i}^{1}\left(\mathrm{e}^{\mathrm{j}\theta_{k_i}} - \mathrm{e}^{\mathrm{j}\theta_{\hat{k}_i}}\right) + \boldsymbol{\eta}_{2,i}\right\|_F^2\right\} < \sum_{i=1}^{z}\left\{\|\boldsymbol{\eta}_{1,i}\|_F^2 + \|\boldsymbol{\eta}_{2,i}\|_F^2\right\}\right) \tag{4.14}$$

The expression in (4-14) may be further simplified as (see Appendix A for derivation)

$$P(t_{k\to g} \to \hat{t}_{k\to g}|\boldsymbol{H}_1\boldsymbol{H}_2) = Q\left(\sqrt{\sum_{i=1}^{z}\kappa_{1,i} + \kappa_{2,i}}\right) \tag{4.15}$$

where $Q(\delta) = \int_{\delta}^{\infty}\frac{1}{2\pi}e^{t^2/2}dt$, and $\kappa_{l,i}$, $l \in [1\colon 2]$, $i \in [1\colon z]$ are central chi-squared RVs with $2N_{\mathrm{R}}$ degrees of freedom, and are defined as [17]:

$$\kappa_{l,i} = \sum_{n=1}^{2N_{\mathrm{R}}}\alpha_{l,i}^2 \qquad i \in [1\colon z], l \in [1\colon 2] \tag{4.16}$$

where, $\sigma_{\alpha_{1,i}}^2 = \frac{\rho}{8z}\left|x_{r_i}^2\right|^2 d_i$, $\sigma_{\alpha_{2,i}}^2 = \frac{\rho}{8z}\left|\bar{x}_{q_i}^1\right|^2 d_i$, d_i is given in Appendix A. Applying the trapezoidal approximation to the Q-function yields a closed form expression given as [29]:

$$Q(\delta) = \frac{1}{2n}\left(\frac{1}{2}\mathrm{e}^{\left(\frac{-\delta^2}{2}\right)} + \sum_{j=1}^{n-1}\exp\left(\frac{-\delta^2}{2\sin^2\left(\frac{j\pi}{2n}\right)}\right)\right) \tag{4.17}$$

The probability density function (PDF) of $\kappa_{l,i}$, $i \in [1\colon z]$, $l \in [1\colon 2]$ is defined as [17]:

$$f_{\kappa_{l,i}}(v_{l,i}) = \frac{1}{\left(2\sigma^2_{\alpha_{l,i}}\right)^{N_R}(N_R-1)!}\exp\left(\frac{-v_{l,i}}{2\sigma^2_{\alpha_{l,i}}}\right) \tag{4.18}$$

Integrating the conditional PEP in (4.15) over all i.i.d. RVs $\kappa_{l,i}$, $i \in [1:z], l \in [1:2]$, then substituting a trapezoidal approximation of the Q-function given in (4-17) and finally, applying the moment generating functions (MGF) $M_i(s)$ of RVs defined as [17]:

$$M_{l,i}(s) = \int_0^\infty f_{\kappa_{l,i}}(v_{l,i}) e^{-sv_{l,i}}\, dv_{l,i} = \left(\frac{1}{1+2\sigma^2_{\alpha_{l,i}}s}\right)^{N_R} \tag{4.19}$$

we arrive at the PEP expression, given by:

$$P\left(t_{k\to g} \to \hat{t}_{k\to g}\right) =$$

$$\frac{1}{2n}\left(\frac{1}{2}\prod_{i=1}^{z} M_{1,i}\left(\frac{1}{2}\right) M_{2,i}\left(\frac{1}{2}\right) + \sum_{k=1}^{n-1}\prod_{i=1}^{z} M_{1,i}\left(\frac{1}{2\sin^2\left(\frac{k\pi}{2n}\right)}\right) M_{2,i}\left(\frac{1}{2\sin^2\left(\frac{k\pi}{2n}\right)}\right)\right) \tag{4.20}$$

The expression in (4.20) may be further expanded as:

$$\begin{aligned} &P\left(t_{k\to g} \to \hat{t}_{k\to g}\right) \\ &\quad = \frac{1}{2n}\left(\frac{1}{2}\prod_{i=1}^{z}\left(\frac{8z}{8z+\rho\left|x^2_{r_i}\right|^2 d_i}\right)^{N_R}\left(\frac{8z}{8z+\rho\left|\bar{x}^1_{q_i}\right|^2 d_i}\right)^{N_R}\right. \\ &\quad \left. + \sum_{k=1}^{n-1}\prod_{i=1}^{z}\left(\frac{8z\sin^2\left(\frac{k\pi}{2n}\right)}{8z\sin^2\left(\frac{k\pi}{2n}\right)+\rho\left|x^2_{r_i}\right|^2 d_i}\right)^{N_R}\left(\frac{8z\sin^2\left(\frac{k\pi}{2n}\right)}{8z\sin^2\left(\frac{k\pi}{2n}\right)+\rho\left|\bar{x}^1_{q_i}\right|^2 d_i}\right)^{N_R}\right) \end{aligned} \tag{4.21}$$

The PEP in (4.21) is substituted into (4.11) and (4.12).

4.4 Simulation and Analytical Results

In this section the simulation and analytical results for $2 \times N_R$ E-USTLD and $2 \times N_R$ USTLD over i.i.d. Rayleigh frequency-flat fast fading channels are presented and compared for the following modulation schemes and additional bit numbers (d):

1. 16-QAM with $d = 1$

2. 64-QAM with $d = 1$

3. 16-QAM with $d = 2$

4. 64-QAM with $d = 2$

The aim of this section is to:

a. Demonstrate that the more bandwidth efficient E-USTLD system retains the BER performance of the conventional USTLD.
b. Evaluate the average BEP to investigate the tightness between simulation and analytical results.

Monte Carlo simulations were performed for both E-USTLD and USTLD, where the average BER is plotted against the average SNR. All BER performance comparisons are made at a BER value of 10^{-6}. For simulation purposes, the fading channel and noise parameters were defined in line with those presented in (4.1) and (4.2) of Section 4.1. Labeling maps are as illustrated in Govindasamy et al [11] (see Appendix B). We also assumed that $N_{\mathrm{R}} = 4; N = 100$; the CSI is known at the receiver; there is sufficient separation of transmit antennas such that all channel gains are independent of each other; MRC reception is employed.

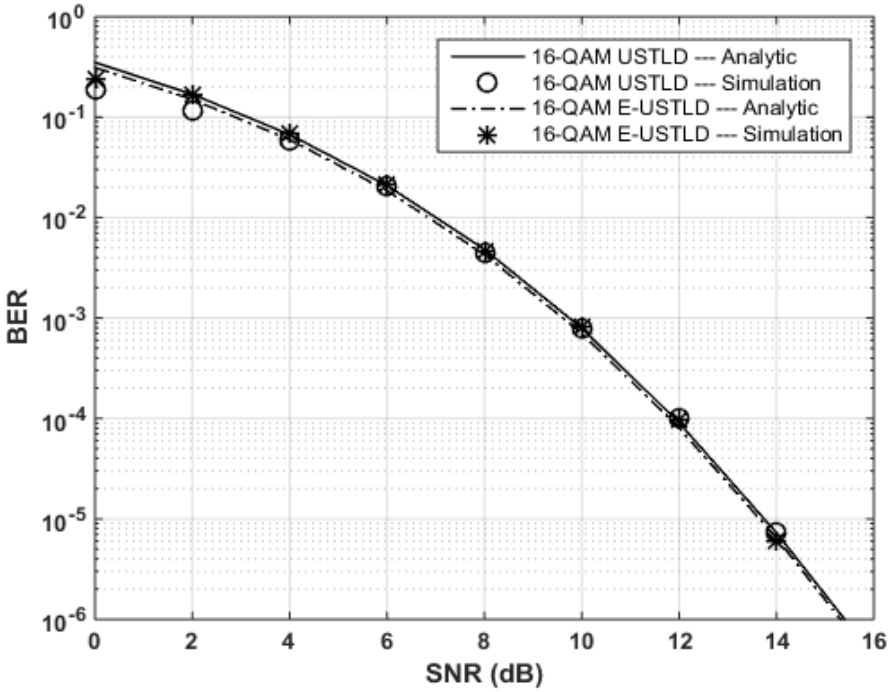

Figure 4-3: BER performance of E-USTLD and USTLD systems for 16-QAM, d = 1 with analytic bounds.

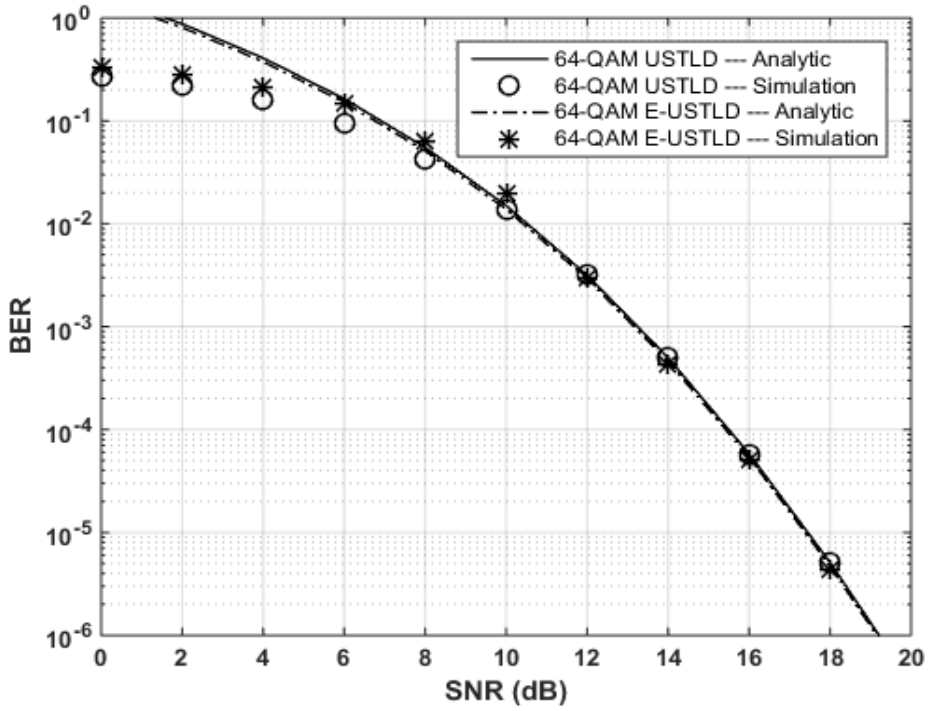

Figure 4-4: BER performance of E-USTLD and USTLD systems for 64-QAM, $d = 1$ with analytic bounds.

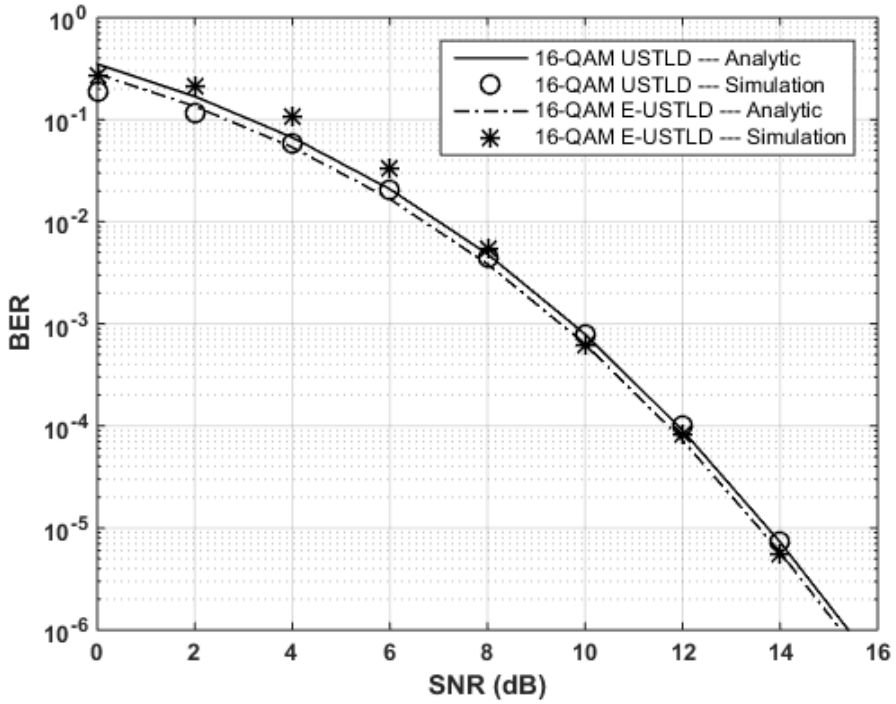

Figure 4-5: BER performance of E-USTLD and USTLD systems for 16-QAM, $d = 2$ with analytic bounds.

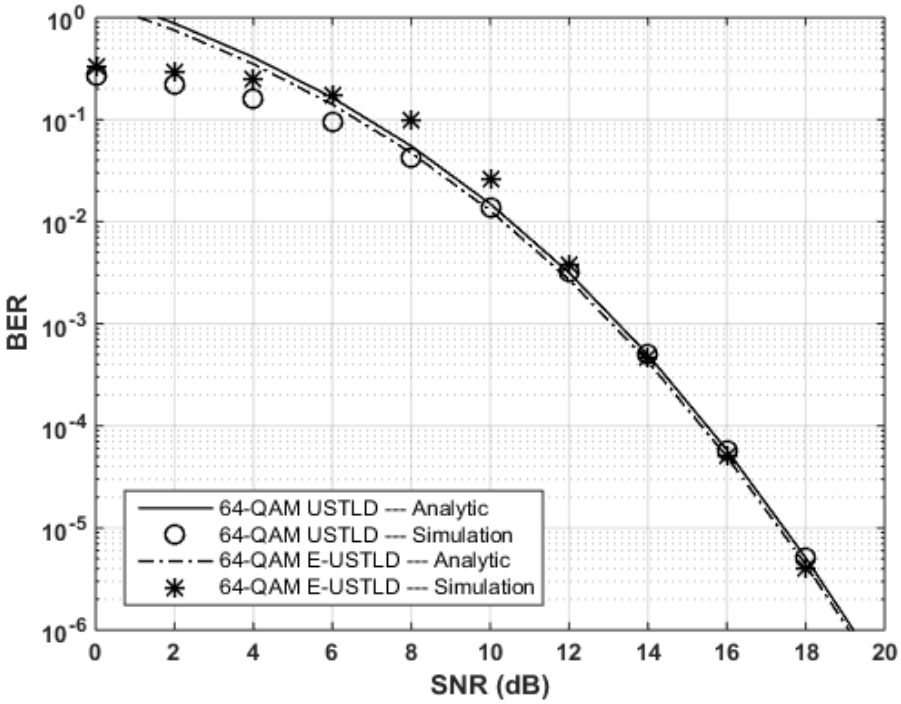

Figure 4-6: BER performance of E-USTLD and USTLD systems for 64-QAM, d = 2 with analytic bounds.

Note that due to a prohibitively large number of calculations involved in determining P_t for 64-QAM E-USTLD scheme with one additional bit, the average BEP P_e for 64-QAM E-USTLD with $d = 1$ is approximated by the dominant P_b. In all cases, the presented analytical results show a tight fit with the simulation results demonstrated for E-USTLD at high SNR. Results presented in Figure 4-3 and Figure 4-4 show that the proposed E-USTLD with one additional bit for 16-QAM and 64-QAM, respectively, retains the error performance of USTLD [17].

A marginal improvement in error performance ($\ll$ 0.5dB) is observed in Figure 4-5 and Figure 4-6 for E-USTLD with two additional bits for 16-QAM and 64-QAM, respectively. Meanwhile, the E-USTLD system achieves better bandwidth efficiency in comparison to the conventional USTLD system as shown in Table 4-2.

For example, the 16-QAM E-USTLD system realises a 12.5% increase in the bandwidth efficiency for each additional bit sent with the transmitted high-rate codeword, while the 64-QAM E-USTLD scheme realises 8.3%. Note that the improvement in the bandwidth efficiency is at the cost of a much higher computational complexity at the receiver since a more complex detector algorithm is employed.

Table 4-2: Bandwidth efficiency comparison of E-USTLD and USTLD.

Scheme	**Bandwidth Efficiency (b/s/Hz)**	**Percentage (%) Increase**
16-QAM USTLD [17]	4	-
16-QAM E-USTLD with d=1	4.5	12.5
16-QAM E-USTLD with d=2	5	25
64-QAM USTLD [17]	6	-
64-QAM E-USTLD with d=1	6.5	8.3
64-QAM E-USTLD with d=2	7	16.7

4.5 Chapter Summary and Conclusion

In this chapter, the trellis code-aided bandwidth efficiency improvement technique was applied to USTLD in the form of the $2 \times N_{\mathrm{R}}$ high-rate USTLD, referred to as E-USTLD. The E-USTLD system exploits the expansion of space-time codes via unitary matrix transformation and good error performance of trellis code-aided schemes, that results in enhanced bandwidth efficiency and the retention of the error performance of the conventional USTLD under the same fading channel and AWGN conditions. A theoretical closed-form lower-bound was formulated for E-USTLD over i.i.d. Rayleigh frequency flat fading channels and it tightly matches the Monte Carlo simulation results at high SNR. It was found that minimum bandwidth efficiency increases of 12.5% and 8.3% were realised for the 16-QAM and 64-QAM E-USTLD schemes, respectively.

However, the bandwidth efficiency is enhanced at the expense of a much higher computational complexity at the receiver. In the next chapter, the OP-based LC near-ML detection scheme developed for the conventional USTLD is extended to the VA detector of the E-USTLD system.

5. Orthogonal Projection Based Near-optimal Viterbi Detection Scheme

As demonstrated in Section 4.1, the VA based detector implements the ML estimation process to compute branch metrics for all possible trellis state transitions. Moreover, the detector also makes an exhaustive search over all allowed USTLD codeword sequences (trellis paths) to estimate the transmitted codeword sequence (survivor path). Consequently, the bandwidth efficiency advantage of the E-USTLD system over the USTLD system is achieved at the cost of a much higher computational complexity at the receiver. In order to reduce the magnitude of increase in computational complexity, we extend the OP based LC near-ML detection scheme formulated for the USTLD system [11] to the computation of branch metrics for E-USTLD in this chapter. The branch metric value represents the difference between the received codeword and the expected codeword along the given trellis path. The larger the value, the less likely the Viterbi decoder is on the right path in the trellis [30].

5.1 Adaptation of LC near-ML Detection Scheme for Branch Metric Computation

In this section, the LC near-ML detection scheme developed in [11] is adapted for branch metric computations in E-USTLD. At each decoding segment, the VA based detection process first independently estimates the most likely candidates for the transmitted symbols x_q^1 and x_r^2 for each trellis state transition. Note that the rotational angle θ_k associated with each trellis state transition is always known. Thereafter the detection process uses the ML detector to estimate the transmitted symbols from among the candidates.

Firstly, we expand the received signals expressions in (4.1) and (4.2) as:

$$\boldsymbol{y}_1 = \sqrt{\frac{\rho}{2}}\, \boldsymbol{h}_1^1 x_q^1 + \sqrt{\frac{\rho}{2}}\, \boldsymbol{h}_1^2 x_r^2 \mathrm{e}^{\mathrm{j}\theta_k} + \boldsymbol{\eta}_1 \tag{5.1}$$

$$\boldsymbol{y}_2 = \sqrt{\frac{\rho}{2}}\, \boldsymbol{h}_2^1 \bar{x}_r^2 + \sqrt{\frac{\rho}{2}}\, \boldsymbol{h}_2^2 \bar{x}_q^1 \mathrm{e}^{\mathrm{j}\theta_k} + \boldsymbol{\eta}_2 \tag{5.2}$$

where $\boldsymbol{h}_i^t$ is an $N_\mathrm{R} \times 1$ vector of the channel fading coefficients from the i^{th} transmit antenna to the N_R receiver antennas for time slot t where $i, t \in [1\colon 2]$, $x_q^1, x_r^2 \in \boldsymbol{\Omega}_M$ and $\bar{x}_q^1, \bar{x}_r^2 \in \lambda(\boldsymbol{\Omega}_M)$ as defined in Section 2.3.

Thereafter, the OP based detection algorithm that was developed for USTLD in [11] is adapted for branch metric computations instead of the method in (4.3), hence, the detection algorithm proceeds through the following steps:

At each decoding segment, Step 1 defines projection matrices $\boldsymbol{P}_i^t$, which, respectively, project a signal on the subspace orthogonal to $\boldsymbol{h}_i^t$ such that $\boldsymbol{P}_i^t \boldsymbol{h}_i^t = 0$. The projection matrices $\boldsymbol{P}_i^t$ are given by:

$$\boldsymbol{P}_i^t = I_{N_\mathrm{R}} - \boldsymbol{h}_i^t \left(\left(\boldsymbol{h}_i^t\right)^H \boldsymbol{h}_i^t \right)^{-1} \left(\boldsymbol{h}_i^t\right)^H \tag{5.3}$$

Thereafter all possible projection subspaces are computed as follows:

$$\boldsymbol{r}_{1,q}^1 = \boldsymbol{y}_1 - \sqrt{\rho/2}\, \boldsymbol{h}_1^1 x_q^1 \tag{5.4}$$

$$\boldsymbol{r}_{2,r}^1 = \boldsymbol{y}_1 - \sqrt{\rho/2}\, \boldsymbol{h}_2^1 x_r^2 \mathrm{e}^{\mathrm{j}\theta_k} \tag{5.5}$$

$$\boldsymbol{r}_{1,r}^2 = \boldsymbol{y}_2 - \sqrt{\rho/2}\, \boldsymbol{h}_1^2 \bar{x}_r^2 \tag{5.6}$$

$$\boldsymbol{r}_{2,q}^2 = \boldsymbol{y}_2 - \sqrt{\rho/2}\, \boldsymbol{h}_2^2 \bar{x}_q^1 \mathrm{e}^{\mathrm{j}\theta_k} \tag{5.7}$$

where $x_q^1, x_r^2 \in \boldsymbol{\Omega}_M$, $\bar{x}_q^1, \bar{x}_r^2 \in \lambda(\boldsymbol{\Omega}_M)$ and $k \in [0: 2^{d+1} - 1]$. Let $\boldsymbol{r}_{t,q}^i, \boldsymbol{r}_{t,r}^i \in \boldsymbol{\mathcal{R}}$ as in Section 2.3, where $i, t \in [1:2]$ and $q, r \in [1:M]$.

Step 2 respectively, selects l_1 and l_2 candidate symbols for x_q^1 and x_r^2 with the smallest projection norms according to (5.8) and (5.9), where $l_1 l_2 < M^2$.

$$\hat{x}_q^1 = \underset{\boldsymbol{r}_{1,q}^1, \boldsymbol{r}_{2,q}^2 \in \boldsymbol{\mathcal{R}}}{\operatorname{argmin}} \left\| \boldsymbol{P}_2^1 \boldsymbol{r}_{1,q}^1 + \boldsymbol{P}_1^2\, \boldsymbol{r}_{2,q}^2 \right\|_F^2 \quad q \in [1:M] \tag{5.8}$$

$$\hat{x}_r^2 = \underset{\boldsymbol{r}_{2,r}^1, \boldsymbol{r}_{1,r}^2 \in \boldsymbol{\mathcal{R}}}{\operatorname{argmin}} \left\| \boldsymbol{P}_1^1 \boldsymbol{r}_{2,r}^1 + \boldsymbol{P}_2^2\, \boldsymbol{r}_{1,r}^2 \right\|_F^2 \quad r \in [1:M] \tag{5.9}$$

The chosen candidates for x_q^1 and x_r^2 are stored in candidate sets $\boldsymbol{z}_q$ and $\boldsymbol{z}_r$ presented below.

$$\boldsymbol{z}_q = \left\{ x_{\hat{q},1}^1\, x_{\hat{q},2}^1 \ldots\, x_{\hat{q},l_1}^1 \right\}\ l_1 < M \tag{5.10}$$

$$\boldsymbol{z}_r = \left\{ x_{\hat{r},1}^2\, x_{\hat{r},2}^2 \ldots\, x_{\hat{r},l_2}^2 \right\}\ l_2 < M \tag{5.11}$$

where $x_{\hat{q},n_1}^1, x_{\hat{r},n_2}^2 \in \boldsymbol{\Omega}_M$, $n_1 \in [1:l_1]$, $n_2 \in [1:l_2]$

Step 3 computes the minimum branch metric $bm_n^{i,l}$ for each possible state i to state l transition by performing an ML search through the elements of the candidate sets $\boldsymbol{z}_q$ and $\boldsymbol{z}_r$ as shown in (5.12).

$$bm_n^{i,l} = \underset{\substack{x_{\hat{q},n_1}^1, x_{\hat{r},n_2}^2 \\ \bar{x}_{\hat{q},n_1}^1, \bar{x}_{\hat{r},n_2}^2}}{\operatorname{argmin}} \left\{ \begin{matrix} \left\| \boldsymbol{y}_1 - \sqrt{\rho/2}\, \boldsymbol{h}_1^1 x_{\hat{q},n_1}^1 - \sqrt{\rho/2}\, \boldsymbol{h}_2^1 x_{\hat{r},n_2}^2 \mathrm{e}^{\mathrm{j}\theta_k} \right\|_F^2 \\ + \left\| \boldsymbol{y}_2 - \sqrt{\rho/2}\, \boldsymbol{h}_1^2 \bar{x}_{\hat{r},n_2}^2 - \sqrt{\rho/2}\, \boldsymbol{h}_2^2 \bar{x}_{\hat{q},n_1}^1 \mathrm{e}^{\mathrm{j}\theta_k} \right\|_F^2 \end{matrix} \right\} \tag{5.12}$$

where $x^1_{\hat{q},n_1} \in \boldsymbol{z}_q,\ x^2_{\hat{r},n_2} \in \boldsymbol{z}_r,\ x^1_{\hat{q},n_1} \in \lambda(\boldsymbol{z}_q),\ x^2_{\hat{r},n_2} \in \lambda(\boldsymbol{z}_r),\ n_1 \in [1{:}\, l_1],\ n_2 \in [1{:}\, l_2],\ i, l \in [0{:}\, 2^{d+1} - 1]$.

5.2 Simulation and Analytical Results: BER Performance between the ML and OP Based Viterbi Detector

In this section, simulation and analytical results are presented for the ML and OP based near-optimal Viterbi detector proposed for E-USTLD in Sections 5.1. The results for the E-USTLD system are presented for the following modulation schemes and additional bit numbers (d):

1. 16-QAM with $d = 1$

2. 64-QAM with $d = 1$

3. 16-QAM with $d = 2$

4. 64-QAM with $d = 2$

The aim of this section is to verify that the BER performance of the OP based near-optimal Viterbi detection scheme attains near optimum BER performance for E-USTLD. Monte Carlo simulations were performed for both E-USTLD and USTLD, where the average BER is plotted against the average SNR. All BER performance comparisons are made at a BER value of 10^{-5}. For simulation purposes, the fading channel and noise parameters were defined in line with those presented in (4.1) and (4.2) of Section 4.1. Labeling maps are as illustrated in Govindasamy et al [11] (see Appendix B). We also assumed that $N_{\mathrm{R}} = 4; N = 100; l_1 = 8;\ l_2 = 6;$ the CSI is known at the receiver; there is sufficient separation of transmit antennas such that all channel gains are independent of each other; MRC reception is employed; there is equal transmit power for all transmissions.

It is evident from Figure 5-1 and Figure 5-2 that the proposed OP based Viterbi detection scheme reaches the optimal BER performance for 16-QAM and 64-QAM with $d = 1$. The results presented in Figure 5-3 and Figure 5-4 show that the proposed detection scheme for 16-QAM and 64-QAM with $d = 2$ approaches the optimal BER performance at all SNR values.

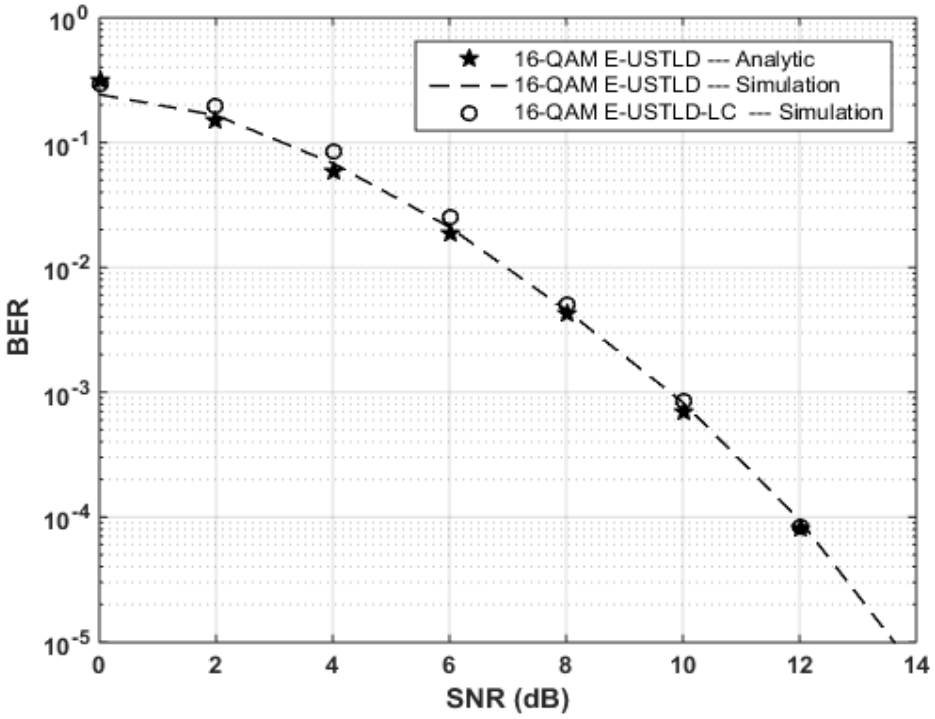

Figure 5-1: Comparison of BER performance for 16-QAM E-USTLD, $d = 1, l_1 = 8, l_2 = 6$ using the ML and the OP based near-optimal Viterbi detectors with analytic bounds.

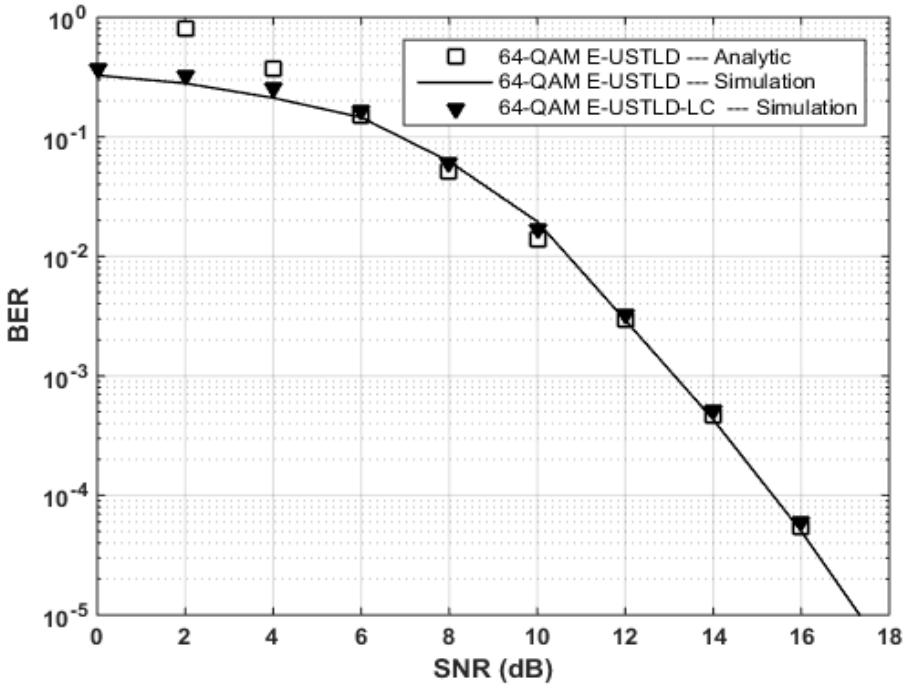

Figure 5-2: Comparison of BER performance for 64-QAM E-USTLD, $d = 1, l_1 = 8, l_2 = 6$ using the ML and the OP based near-optimal Viterbi detectors with analytic bounds.

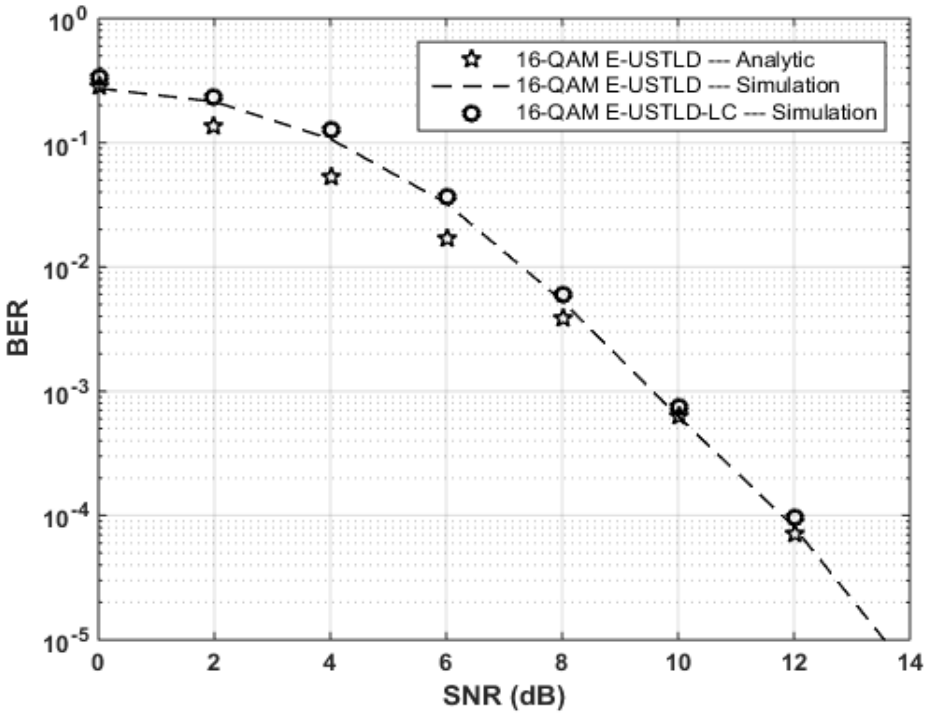

Figure 5-3: Comparison of BER performance for 16-QAM E-USTLD, $d = 2, l_1 = 8, l_2 = 6$ using the ML and the OP based near-optimal Viterbi detectors with analytic bounds.

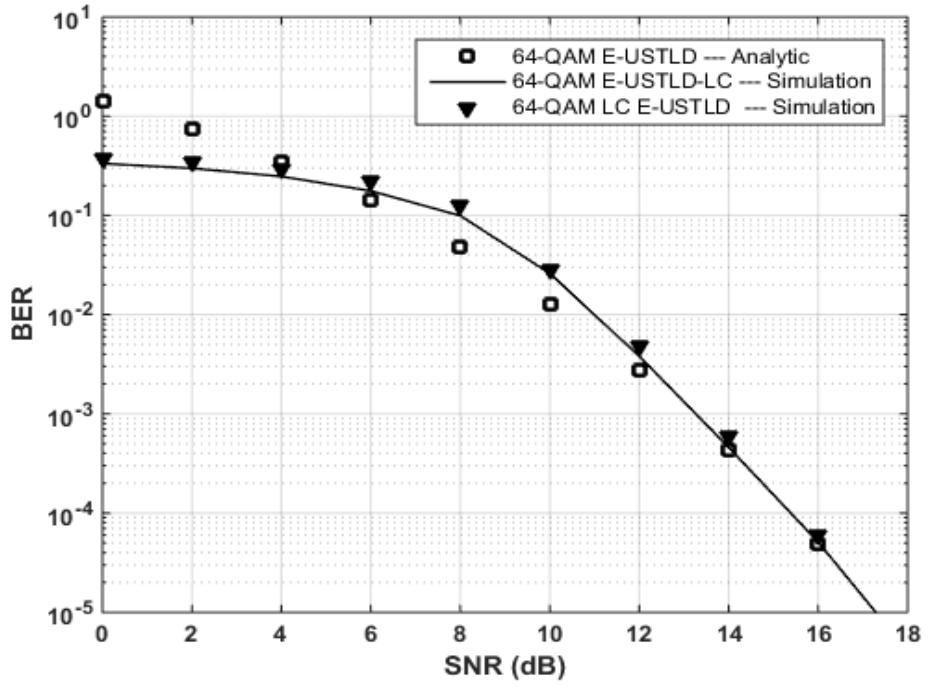

Figure 5-4: Comparison of BER performance for 64-QAM E-USTLD, $d = 2, l_1 = 8, l_2 = 6$ using the ML and the OP based near-optimal Viterbi detectors with analytic bounds.

5.3 Chapter Summary and Conclusion

In this chapter, the OP based LC near-ML detection scheme developed for USTLD was extended to E-USTLD in the form of OP based near-optimal Viterbi detection scheme. The presented simulation results verify that the proposed OP based near-optimal Viterbi detector approaches the optimum BER performance at all SNR values for various square M-QAM modulation schemes and additional bit numbers.

6. Conclusion

This chapter summarises the research contributions, suggests future research regarding the trellis code-aided bandwidth efficiency improvement technique for space-time block coded communication systems and draws concluding remarks from presented work.

6.1 Research Contributions

The research contributions are as follows:

Firstly, a differentially transmitted high-rate STBC system dubbed TC-DSTBC, which achieves a bandwidth efficiency advantage over the conventional differential Alamouti system, was investigated. The fundamental idea of TC-DSTBC is to employ a dynamic mapping rule to map additional bits onto the unitary matrix transformation expanded Alamouti STBC prior to differential encoding. A trellis code-aided bandwidth efficiency improvement technique that incorporates trellis coding into the mapping of additional bits to the expanded STBC was proposed for square M-QAM over i.i.d. Rayleigh frequency-flat quasi-static fading channels. The percentage bandwidth efficiency advantage of the TC-DSTBC over the conventional Alamouti DSTBC is tabulated in Table 6-1. Furthermore, Monte Carlo simulation results show that the proposed TC-DSTBC system retains the BER performance of the conventional Alamouti DSTBC under the same fading channel and noise conditions.

Table 6-1: Bandwidth efficiency advantage of TC-DSTBC over the conventional Alamouti DSTBC

Modulation scheme and number of additional bits	**Percentage (%) advantage**
16-QAM TC-DSTBC with d=1	12.5
16-QAM TC-DSTBC with d=2	25
64-QAM TC-DSTBC with d=1	8.3
64-QAM TC-DSTBC with d=2	16.7

Secondly, the extension of the trellis code-aided bandwidth efficiency improvement technique to USTLD was investigated, and hence a new high-rate USTLD system called E-USTLD was proposed. Monte Carlo simulations were performed for USTLD and E-USTLD for various square M-QAM modulation orders and numbers of additional bits over i.i.d. Rayleigh frequency-flat fast fading channels. The simulation results show that the proposed E-USTLD with one additional bit retains the BER performance of the conventional USTLD at high SNR. A marginal improvement in BER performance (of less than 0.5dB) is achieved as the bandwidth efficiency increases. Furthermore, a closed-form lower bound on the BER for E-USTLD was derived for i.i.d. Rayleigh

frequency-flat fading channels, and the lower bound made a tight fit with the simulation results at high SNR.

Lastly, it was noted from system implementation that the bandwidth efficiency improvement is achieved at the cost of a much higher computational complexity at the receiver, therefore, the orthogonal projection (OP) based LC near-ML detection scheme developed for USTLD by Govindasamy et al [11] was integrated with the Viterbi algorithm (VA) of the E-USTLD detection scheme in order to reduce the magnitude of increase in the computational complexity. The presented Monte Carlo simulation results show that the E-USTLD with the modified Viterbi detection scheme converges to the optimal BER performance at all SNR values for the various square M-QAM modulation schemes and additional bit numbers.

6.2 Future Research

The bandwidth efficiency improvement technique presented in this dissertation can be extended to other space-time block coded transmission systems with minor modifications. The presented work has also opened other research avenues as denoted by research topics mentioned below.

6.2.1 Low-complexity Viterbi Detection

In this dissertation, we employed a high-complexity VA based detection scheme that implements the ML estimation process to compute branch metrics for all possible trellis state transitions. Although a modified Viterbi algorithm (VA) that implements LC near-ML detection has been developed for E-USTLD, the detection complexity is still high since the VA detector employs ML sequence estimation (MLSE) i.e. the VA detector makes an exhaustive search over all possible high-rate codeword sequences to determine the most likely transmitted codeword sequence. Hence, research should be conducted to develop Viterbi detection techniques with less complex algorithms.

6.2.2 Trellis Code-aided Space-time Block Codes in Correlated Fading Channels

The error performance of high-rate space-time block coded wireless systems has been comprehensively investigated for statistically independent channels. However, insufficient spacing of antenna or lack of scattering environments in practical wireless communications may result in correlated channels [31]. Hence, future research should be aimed at investigating and documenting the error performance of trellis code-aided high-rate space-time coded systems in correlated channels.

6.2.3 Trellis Code-aided Space-time Channel Modulation

Space-time channel modulation (STCM) is a recent high-rate scheme that extends the conventional Alamouti STBC into the channel state dimension. Documented performance results

show that STCM schemes can achieve superior BER performance to that of the conventional Alamouti STBC [32]. Consequently, the STCM scheme is a suitable transmission scheme for future communication systems. In order to make STCM more attractive as a transmission scheme for multiple antenna communication systems, future research should focus on the optimal application of the trellis code-aided bandwidth efficiency improvement technique to STCM.

6.2.4 Performance Analysis of Coherent Trellis Code-aided Space-time Block Codes with Channel Estimation Errors

In this dissertation, results presented for E-USTLD show a possible high communications link reliability. E-USTLD requires perfect CSI to be known at the receiver in order to detect the transmitted information [33]. In practical communication systems the CSI is estimated with errors due to channel imperfections. Channel state estimation errors impact negatively on the link reliability, hence, future research should investigate the suitability of E-USTLD to meet demands of future communication systems by assessing the error performance of E-USTLD under various channel state estimation error conditions.

6.3 Concluding Remarks

In this dissertation, a trellis code-aided bandwidth efficiency improvement technique that improves the bandwidth efficiency of space-time block coded wireless communication systems without compromising the link reliability (error performance) has been presented. The presented technique has been investigated for differentially transmitted Alamouti STBC in the form of TC-DSTBC, and for USTLD in the form of E-USTLD. The significance of the trellis code-aided bandwidth efficiency improvement technique for space-time block coded systems is that it addresses the high speed data demands of modern digital communication systems. However, the bandwidth efficiency improvement has been achieved at the cost of high detection complexity, hence, an OP based LC near-optimal detection scheme for E-USTLD has been presented. Moreover, the work presented in this dissertation has opened other avenues for future research.

Appendix A

The E-USTLD signals received prior to each decoding segment i are expressed as:

$$\boldsymbol{y}_{1,i} = \sqrt{\frac{\rho}{2}}\, \boldsymbol{h}_{1,i}^{1} x_{q_i}^{1} + \sqrt{\frac{\rho}{2}}\, \boldsymbol{h}_{1,i}^{2} x_{r_i}^{2} \mathrm{e}^{\mathrm{j}\theta_{k_i}} + \boldsymbol{\eta}_{1,i} \tag{A.1}$$

$$\boldsymbol{y}_{2,i} = \sqrt{\frac{\rho}{2}}\, \boldsymbol{h}_{2,i}^{1} \bar{x}_{r_i}^{2} + \sqrt{\frac{\rho}{2}}\, \boldsymbol{h}_{2,i}^{2} \bar{x}_{q_i}^{1} \mathrm{e}^{\mathrm{j}\theta_{k_i}} + \boldsymbol{\eta}_{2,i} \tag{A.2}$$

Assuming that all symbol pairs are detected correctly, while the encoding trellis path is detected with errors, the PEP conditioned on $\boldsymbol{H}_1$ and $\boldsymbol{H}_2$ can be expressed as:

$$P\left(t_{k\to g} \to \hat{t}_{k\to g} | \boldsymbol{H}_1 \boldsymbol{H}_2\right) = P\left(\sum_{i=1}^{z} \left\{ \left\| \boldsymbol{y}_{1,i} - \sqrt{\frac{\rho}{2}}\, \boldsymbol{h}_{1,i}^{1} x_{q_i}^{1} - \sqrt{\frac{\rho}{2}}\, \boldsymbol{h}_{2,i}^{1} x_{r_i}^{2} \mathrm{e}^{\mathrm{j}\theta_{\hat{k}_i}} \right\|_F^2 + \right.\right.$$
$$\left.\left. \left\| \boldsymbol{y}_{2,i} - \sqrt{\frac{\rho}{2}}\, \boldsymbol{h}_{2,i}^{1} \bar{x}_{r_i}^{2} - \sqrt{\frac{\rho}{2}}\, \boldsymbol{h}_{2,i}^{2} \bar{x}_{q_i}^{1} \mathrm{e}^{\mathrm{j}\theta_{\hat{k}_i}} \right\|_F^2 \right\} < \sum_{i=1}^{z} \left\{ \left\| \boldsymbol{y}_{1,i} - \sqrt{\frac{\rho}{2}}\, \boldsymbol{h}_{1,i}^{1} x_{q_i}^{1} - \sqrt{\frac{\rho}{2}}\, \boldsymbol{h}_{2,i}^{1} x_{r_i}^{2} \mathrm{e}^{\mathrm{j}\theta_{k_i}} \right\|_F^2 + \right.\right.$$
$$\left.\left. \left\| \boldsymbol{y}_{2,i} - \sqrt{\frac{\rho}{2}}\, \boldsymbol{h}_{2,i}^{1} \bar{x}_{r_i}^{2} - \sqrt{\frac{\rho}{2}}\, \boldsymbol{h}_{2,i}^{2} \bar{x}_{q_i}^{1} \mathrm{e}^{\mathrm{j}\theta_{k_i}} \right\|_F^2 \right\} \right) \tag{A.3}$$

where z is the length of the shortest error event path. Substituting (A.1) and (A.2) into (A.3) yields:

$$P\left(t_{k\to g} \to \hat{t}_{k\to g} | \boldsymbol{H}_1 \boldsymbol{H}_2\right) = P\left(\sum_{i=1}^{z} \left\{ \left\| \sqrt{\frac{\rho}{2}}\, \boldsymbol{h}_{2,i}^{1} x_{r_i}^{2} \left(\mathrm{e}^{\mathrm{j}\theta_{k_i}} - \mathrm{e}^{\mathrm{j}\theta_{\hat{k}_i}}\right) + \boldsymbol{\eta}_{1,i} \right\|_F^2 + \right.\right.$$
$$\left.\left. \left\| \sqrt{\frac{\rho}{2}}\, \boldsymbol{h}_{2,i}^{2} \bar{x}_{q_i}^{1} \left(\mathrm{e}^{\mathrm{j}\theta_{k_i}} - \mathrm{e}^{\mathrm{j}\theta_{\hat{k}_i}}\right) + \boldsymbol{\eta}_{2,i} \right\|_F^2 \right\} < \sum_{i=1}^{z} \left\{ \left\| \boldsymbol{\eta}_{1,i} \right\|_F^2 + \left\| \boldsymbol{\eta}_{2,i} \right\|_F^2 \right\} \right) \tag{A.4}$$

Let $\boldsymbol{A}_i = \sqrt{\frac{\rho}{2}}\, \boldsymbol{h}_{2,i}^{1} x_{r_i}^{2} \left(\mathrm{e}^{\mathrm{j}\theta_{k_i}} - \mathrm{e}^{\mathrm{j}\theta_{\hat{k}_i}}\right)$ and $\boldsymbol{B}_i = \sqrt{\frac{\rho}{2}}\, \boldsymbol{h}_{2,i}^{2} \bar{x}_{q_i}^{1} \left(\mathrm{e}^{\mathrm{j}\theta_{k_i}} - \mathrm{e}^{\mathrm{j}\theta_{\hat{k}_i}}\right)$. Applying the triangle inequality as in Naidoo et al [28] yields:

$$P\left(t_{k\to g} \to \hat{t}_{k\to g} | \boldsymbol{H}_1 \boldsymbol{H}_2\right)$$
$$= P\left(\sum_{i=1}^{z} \left\{ \|\boldsymbol{A}_i\|_F^2 - \left\| \boldsymbol{\eta}_{1,i} \right\|_F^2 + \|\boldsymbol{B}_i\|_F^2 - \left\| \boldsymbol{\eta}_{2,i} \right\|_F^2 \right\} < \sum_{i=1}^{z} \left\{ \left\| \boldsymbol{\eta}_{1,i} \right\|_F^2 + \left\| \boldsymbol{\eta}_{2,i} \right\|_F^2 \right\} \right) \tag{A.5}$$

Considering that $\boldsymbol{\eta}_{1,i}$ and $\boldsymbol{\eta}_{2,i}$ are random Gaussian vectors with independent entries, the sum $\sum_{i=1}^{z} \left\{ \left\| \boldsymbol{\eta}_{1,i} \right\|_F^2 + \left\| \boldsymbol{\eta}_{2,i} \right\|_F^2 \right\}$ can be written as $\left\| \sum_{i=1}^{z} \left(\boldsymbol{\eta}_{1,i} + \boldsymbol{\eta}_{2,i} \right) \right\|_F^2$. Therefore, (A.5) can be further simplified as:

$$P\left(t_{k\to g} \to \hat{t}_{k\to g}|\boldsymbol{H}_1\boldsymbol{H}_2\right) = P\left(\left\|\sum_{i=1}^{z}\left(\boldsymbol{\eta}_{1,i}+\boldsymbol{\eta}_{2,i}\right)\right\|_F^2 > \sum_{i=1}^{z}\{\|\boldsymbol{A}_i\|_F^2 + \|\boldsymbol{B}_i\|_F^2\}\right)$$

$$= P\left(\left\|\sum_{i=1}^{z}\left(\boldsymbol{\eta}_{1,i}+\boldsymbol{\eta}_{2,i}\right)\right\|_F > \sqrt{\frac{1}{2}\sum_{i=1}^{z}(\|\boldsymbol{A}_i\|_F^2 + \|\boldsymbol{B}_i\|_F^2)}\right) \quad \text{(A.6)}$$

Let $\boldsymbol{\eta}_{\mathrm{T}}$, with entries that are Gaussian RVs distributed as $CN(0,1)$ be defined as:

$$\boldsymbol{\eta}_{\mathrm{T}} = \frac{\sum_{i=1}^{z}(\boldsymbol{\eta}_{1,i}+\boldsymbol{\eta}_{2,i})}{\sqrt{2z}} \quad \text{(A.7)}$$

where $2z$ is the variance of each entry of the sum $\sum_{i=1}^{z}\left(\boldsymbol{\eta}_{1,i}+\boldsymbol{\eta}_{2,i}\right)$. Substituting (A.7) into (A.6) yields:

$$P\left(t_{k\to g} \to \hat{t}_{k\to g}|\boldsymbol{H}_1\boldsymbol{H}_2\right) = P\left(\|\boldsymbol{\eta}_{\mathrm{T}}\|_F > \sqrt{\frac{1}{4z}\sum_{i=1}^{z}(\|\boldsymbol{A}_i\|_F^2 + \|\boldsymbol{B}_i\|_F^2)}\right)$$

$$= Q\left(\sqrt{\frac{1}{4z}\sum_{i=1}^{z}(\|\boldsymbol{A}_i\|_F^2 + \|\boldsymbol{B}_i\|_F^2)}\right)$$

$$= Q\left(\sqrt{\sum_{i=1}^{z}\frac{\rho}{8z}\left\|\boldsymbol{h}_{2,i}^1\right\|_F^2\left|x_{r_i}^2\right|^2 d_i + \frac{\rho}{8z}\left\|\boldsymbol{h}_{2,i}^2\right\|_F^2\left|\bar{x}_{q_i}^1\right|^2 d_i}\right) \quad \text{(A.8)}$$

where $d_i = \left|\mathrm{e}^{\mathrm{j}\theta_{k_i}} - \mathrm{e}^{\mathrm{j}\theta_{\tilde{k}_i}}\right|^2$, $i \in [1{:}\,z]$.

Let $\kappa_{1,i} = \frac{\rho}{8z}\left\|\boldsymbol{h}_{2,i}^1\right\|_F^2\left|x_{r_i}^2\right|^2 d_i$ and $\kappa_{2,i} = \frac{\rho}{8z}\left\|\boldsymbol{h}_{2,i}^2\right\|_F^2\left|\bar{x}_{q_i}^1\right|^2 d_i$, therefore

$$P\left(t_{k\to g} \to \hat{t}_{k\to g}|\boldsymbol{H}_1\boldsymbol{H}_2\right) = Q\left(\sqrt{\sum_{i=1}^{z}\left(\kappa_{1,i}+\kappa_{2,i}\right)}\right) \quad \text{(A.9)}$$

Note that employing trellis code-aided mapping of additional bits, sets the squared distances as $d_1 = 4$, $d_2 = 2$ and $d_3 = 4$ for a scheme with one additional bit and z = 3, while for a scheme with two additional bits, $d_i = 4$; $i \in [1{:}\,z]$ and $z = 2$.

Appendix B

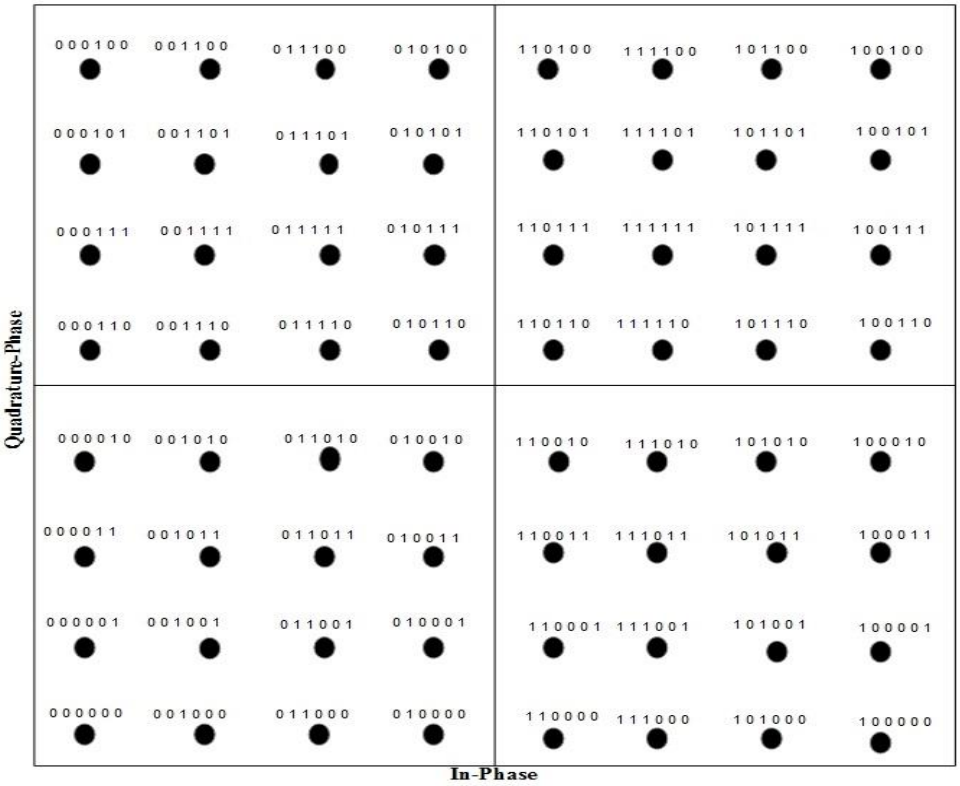

Figure A-1: 64-QAM Gray-coded labeling map ω^G [11]

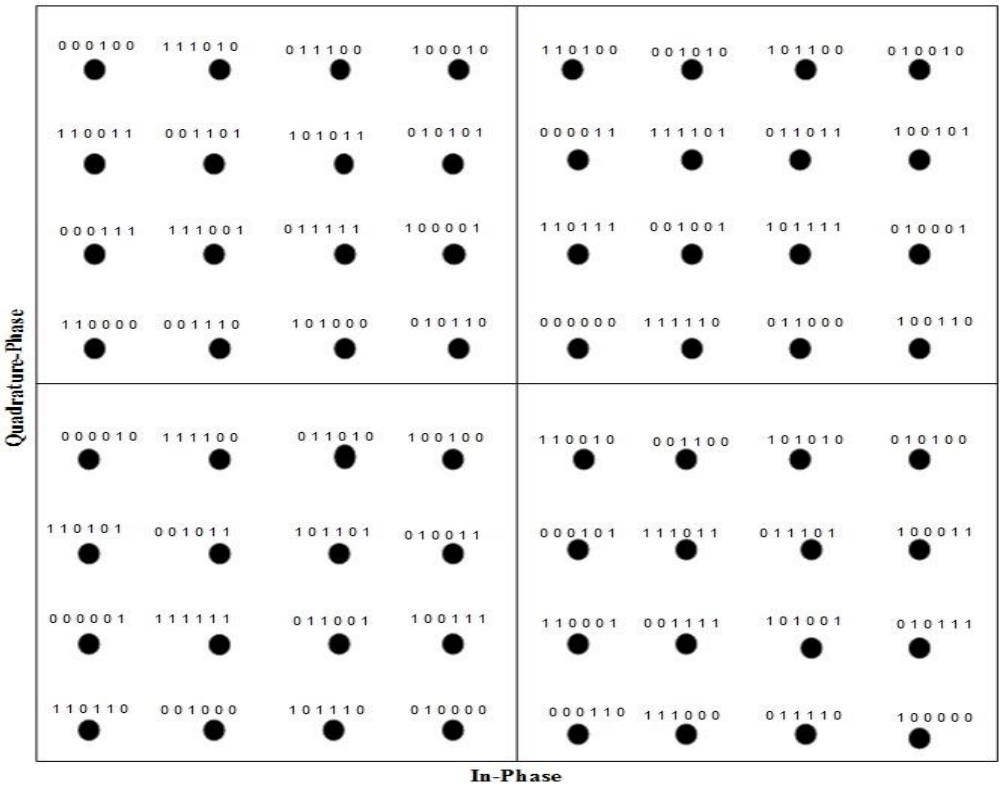

Figure A-2: 64-QAM optimized labeling map ω^O [11]

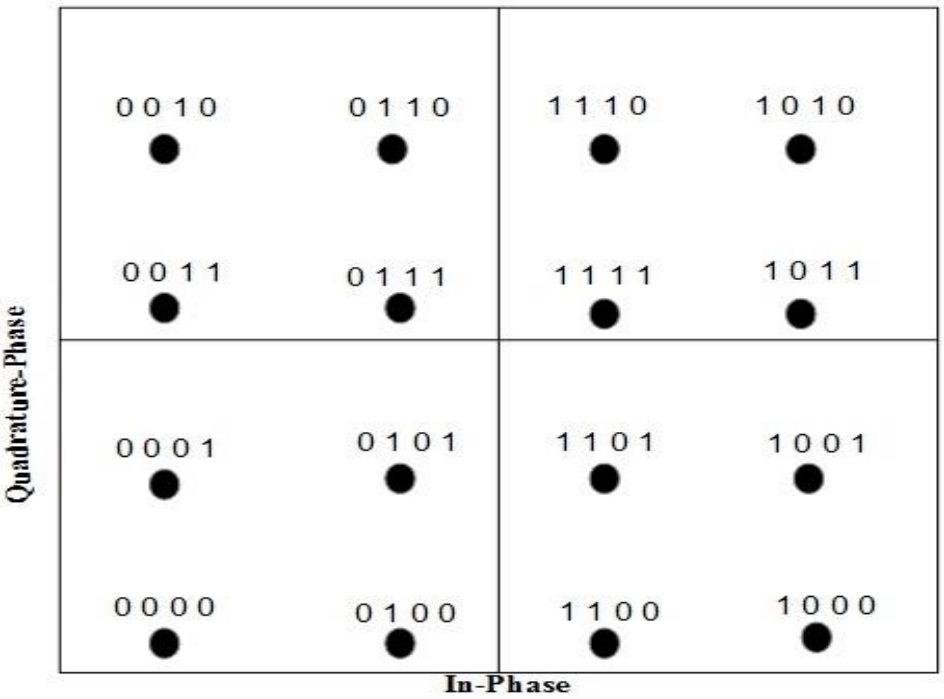

Figure A-3: 16-QAM Gray-coded labeling map ω^G [11]

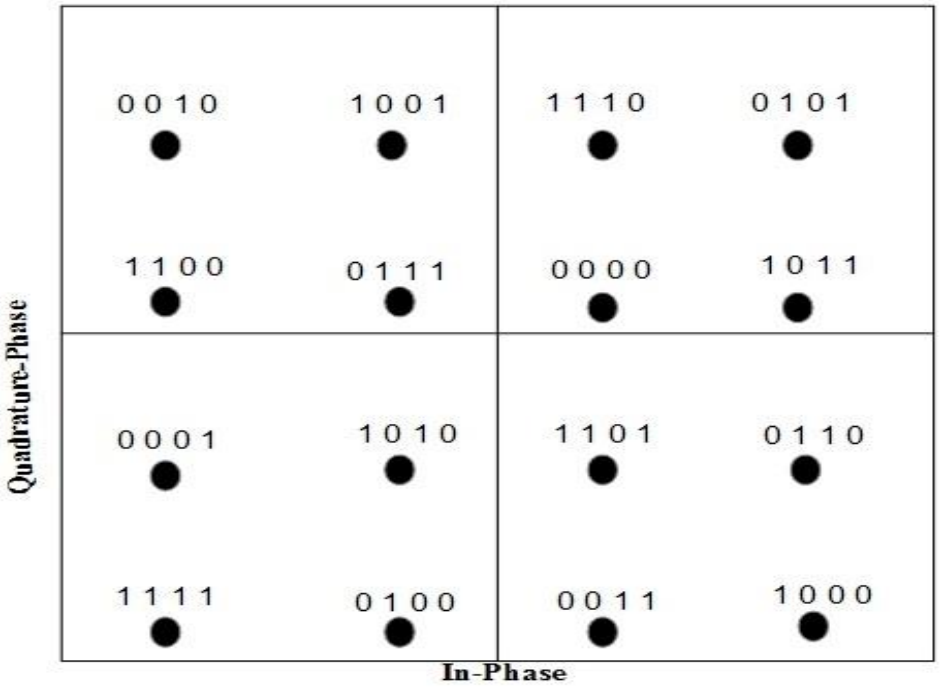

Figure A-4: 16-QAM optimized labeling map ω^O [11]

References

[1] S. K. Roy and N. Jain, "BER performance analysis of Alamouti coding technique in Rayleigh fading channel," *International Journal of Science and Research,* vol. 3, no. 12, pp. 480-483, Dec. 2014.

[2] S. M. Alamouti, "A Simple transmit diversity technique for wireless communications," *IEEE Journal on Selected Areas in Communications,* vol. 16, no. 8, pp. 1451-1458, Oct. 1998.

[3] C. Xu, S. X. N. Li Wang and L. Hanzo, "Multiple-symbol differential sphere detection-aided differential space-time block codes using QAM constellations," *IEEE Signal Processing Letters,* vol. 18, no. 9, pp. 497-500, Sep. 2011.

[4] V. Tarokh and H. Jafarkhani, "A differential detection scheme for transmit diversity," *IEEE Journal on Selected Areas in Communications,* vol. 18, no. 7, pp. 1169-1174, July 2000.

[5] D. Divsalar and M. K. Simon, "Multiple-symbol differential detection of MPSK," *IEEE Transactions on Communications,* vol. 38, no. 3, pp. 300-308, Mar. 1990.

[6] L. Li, Z. Fang, Y. Zhu and Z. Wang, "Generalized differential transmission for STBC systems," in *IEEE Global Telecommunications (GLOBECOM) Conference*, New Orleans, pp. 1-5, Dec. 2008.

[7] E. B. Slimane, S. Jarboui, I. Lamouchi and A. Bouallegue, "Concatenated differential space-time block codes and four dimensional 8-PSK trellis coded modulation for wireless MIMO system with Rayleigh fading noise," *International Journal of Computer Science and Information Technologies,* vol. 3, no. 2, pp. 3456-3459, Apr. 2012.

[8] H. Lee, M. Siti, W. Zhu and M. Fitz, "Super-orthogonal space-time block code using a unitary expansion," in *IEEE 60th Annual Conference on Vehicular Technology*, Los Angeles, vol. 4, pp. 2513-2517, Sep. 2004.

[9] W. T. Chen, "Spectral efficiency analysis for LTE networks," in *IEEE Fourth International Conference on Consumer Electronics*, Berlin, pp. 93-95, Sep. 2014.

[10] E. Basar , U. Aygolu, E. Panayirci and H. V. Poor, "Space-time block coded spatial modulation," *IEEE Transactions on Communications,* vol. 59, no. 3, pp. 823-832, Mar. 2011.

[11] K. Govindasamy, H. Xu and N. Pillay, "Space-time block coded spatial modulation with labeling diversity," *International Journal of Communication Systems,* vol. e3395. https://doi.org/10.1002/dac.3395, 2017.

[12] Q. Ling and T. T. Li, "Efficiency Improvement for Alamouti Codes," in *IEEE 40th Annual Conference on Information Sciences and Systems*, Princeton, pp. 569-572, Mar. 2006.

[13] Z. A. Baloch, M. U. Baloch and N. Hussain, "Efficiency improvement of space time block codes," *International Journal of Communications, Network and System Sciences*, vol. 3, no. 6, pp. 507-510, June 2010.

[14] J. Liu, "Wireless multipath fading channels modeling and simulation based on sum-of-sinsoids," in *First IEEE International Conference on Computer Communication and the Internet*, Wuhan, pp. 165-168, Oct. 2016.

[15] F. E. Mahmood, F. Y. Abdullah and H. A. Al-Tayyar, "Analysis, simulation and modeling of mobile Rayleigh fading channel using Labview," in *IEEE Antenna and Propagation Conference*, Loughborough, pp. 1-6, Nov. 2011.

[16] C. S. Hwang, S. H. Nam, J. Chung and V. Tarokh, "Differential space-time block codes using nonconstant modulus constellations," *IEEE Transactions on Signal Processing,* vol. 51, no. 11, pp. 2955-2964, Nov. 2003.

[17] H. Xu, K. Govindasamy and N. Pillay, "Uncoded space-time labeling diversity," *IEEE Communication Letters,* vol. 20, no. 8, pp. 1511-1514, June 2016.

[18] X. Li, A. Chindapol and J. A. Ritcey, "Bit-interleaved coded modulation with iterative decoding and 8 PSK signaling," *IEEE Transactions on Communications*, vol. 50, no. 8, pp. 1250-1257, Aug. 2002.

[19] Y. Huang and J. A. Ritcey, "Optimal constellation labeling for iteratively decoded bit-interleaved space-time coded modulation," *IEEE Transactions in Information Theory,* vol. 51, no. 5, pp. 1865-1871, May 2005.

[20] M. Krasicki and P. Szulakiewicz, "Boosted space-time diversity scheme for wireless communications," *Electronics Letters,* vol. 45, no. 16, pp. 843-845, July 2009.

[21] E. J. Kaminsky, J. Ayo and K. V. Cartwright, "TCM without constellation expansion," *Journal of Communications and Networks,* vol. 4, no. 2, pp. 90-96, June 2002.

[22] G. Ungerboeck, “Trellis-coded modulation with redundant signal sets,” *IEEE Communication Magazine,* vol. 25, no. 2, pp. 5-21, Feb. 1987.

[23] S. Benedetto, M. Mondin and G. Montorsi, “Performance evaluation of trellis coded modulation schemes,” *Proceedings of the IEEE,* vol. 82, no. 6, pp. 833-855, June 1994.

[24] S. Das, N. Al-Dhahir and R. Calderbank, “Novel full-diversity high-rate STBC for 2 and 4 transmit antennas,” *IEEE Communications Letters,* vol. 10, no. 3, pp. 171-173, Mar. 2006.

[25] H. Xu and N. Pillay, “Simple near-maximum-likelihood low-complexity detection scheme for Alamouti space-time block coded spatial modulation,” *IET Communications,* vol. 8, no. 15, pp. 2611-2618, May 2014.

[26] S. Siwamogsatham and M. F. Fitz, “Improved high rate space-time codes via orthogonality and set partitioning,” in *IEEE Wireless Communication and Networking Conference*, Orlando, vol. 1, pp. 264-270, Mar. 2002.

[27] S. S. H. Bidaki, S. Talebi and M. Shahabinejad, “A full-rate full-diversity 2\times2 space-time block code with linear complexity for the maximum likelihood receiver,” *IEEE Communications Letters,* vol. 15, no. 8, pp. 842-844, Aug. 2011.

[28] N. R. Naidoo, H. Xu and T. Quazi, “Spatial modulation: optimal detector asymptotic performance and multiple-stage detection,” *IET Communications,* vol. 5, no. 10, pp. 1368-1376, July 2011.

[29] Z. Paruk and H. Xu, “Performance analysis and simplified detection for two-dimensional signal space diversity with MRC reception,” *SAIEE Africa Research Journal,* vol. 104, no. 3, pp. 97-106, Sep. 2013.

[30] R. A. Abdallah, S. J. Lee, M. Goel and N. R. Shanbhag, “Low-power pre-coding based Viterbi decoder for tail-biting convolutional codes,” in *Signal Processing Systems*, Tampere, pp. 185-190, Oct. 2009.

[31] A. Hedayat, H. Shah and A. Nosratinia, “Analysis of Space–time coding in correlated fading channels,” *IEEE Transactions on Wireless Communications,* vol. 4, no. 6, pp. 2882-2891, Nov. 2005.

[32] E. Basar and I. Altunbas, “Space-time channel modulation,” *IEEE Transactions on Vehicular Technology,* vol. 66, no. 8, pp. 7609-7614, Aug. 2017.

[33] B. Ahlawat and R. K. Reddy, “Channel estimation and performance evaluation of STBC with channel coding,” *International Journal of Engineering Research & Technology,* vol. 1, no. 3, pp. 1-6, May 2012.